



POLITECNICO DI TORINO

Electrical Engineering
Master degree thesis

**Implementation of a
multithreaded PEEC code for
the study of RF coils in MRI
scanners**

Supervisor
prof. Fabio Freschi

Student
Alberto Scotta

March 2018

Abstract

The thesis aims at developing the calculation kernel for the efficient extraction of the inductive and capacitive coefficients of the partial element equivalent circuit method.

The method will be then applied to the study of a 12-channel RF coil array of a MRI scanner.

Contents

1	Introduction	4
1.1	Maxwell's equations	4
1.2	Constitutive equations	5
1.3	Electric scalar and magnetic vector potential wave equations	6
1.3.1	Solution	7
1.4	Electric field integral equation	8
1.4.1	EFIE for conducting regions	8
1.5	Continuity equation	9
2	Triangular-mesh-based PEEC	10
2.1	Basis functions	11
2.1.1	Current basis functions	11
2.1.2	Charge basis functions	15
2.2	Weak formulation of the problem	16
2.3	Problem discretization	17
2.3.1	Galärkin approach	18
2.3.2	Collocation approach	20
2.4	Equivalent circuit	22
3	Evaluation of circuit elements	24
3.1	Partial resistances	24
3.1.1	Self term	24
3.1.2	Mutual term	25
3.2	Integrals of the Laplace operator Green's function times linear functions on polygonal domains	27
3.3	Partial coefficients of potential	30
3.4	Partial inductances	30
3.4.1	Line integral approximation	31
3.4.2	Magnetic vector potential due to unitary edge current	32

4	Benchmarking	35
4.1	Resistive code	35
4.2	Capacitive code	37
4.3	Inductive code	38
4.4	Quasi-static code	38
4.5	Full-wave code	39
4.6	Mackenzie’s code	41
4.6.1	Inductive code	41
4.7	Frequency sweep artifacts	43
5	Implementation and Performance analysis	46
5.1	Partial element computation	46
5.2	Frequency solution	48
6	RF coils	51
6.1	Microstrip parameters	52
6.2	Microstrip coil design	53
6.3	Coil characterization	54
6.3.1	PEEC results	54
7	Conclusion	59
7.1	Further development	59
A	Divergence of RWG basis functions	60
B	Spice netlist for RF coil simulation	61

Chapter 1

Introduction

In this introductory chapter, some basic EM relationships will be recalled to be used as starting point for the following PEEC development.

1.1 Maxwell's equations

Maxwell's equations, beyond being the fundamental laws of electromagnetics, are the basis of the PEEC method, therefore it is useful to state them beforehand, all at once.

$$\operatorname{div} \mathbf{D} = \rho \quad (1.1)$$

$$\operatorname{div} \mathbf{B} = 0 \quad (1.2)$$

$$\operatorname{curl} \mathbf{E} = -\frac{\partial \mathbf{B}}{\partial t} \quad (1.3)$$

$$\operatorname{curl} \mathbf{H} = \frac{\partial \mathbf{D}}{\partial t} + \mathbf{J} \quad (1.4)$$

The first two equations are named after Carl Friedrich Gauss. They are the electric Gauss's law (1.1) and the magnetic Gauss's law (1.2). Equation 1.3 bears the name of as many as three physicists Faraday, Neumann and Lenz that are credited for it. The fathers of equation 1.4 are Ampère and Maxwell; who contributed each a term of the right-hand side. Maxwell was, as well, the first to write down all of them in a complete form, thus the name of the whole set.

The above equations are general in that the media can be non-homogeneous, non-linear and non-isotropic. They form a set of partial differential equations relating time and space derivatives to charge and current densities.

1.2 Constitutive equations

In isotropic and linear media the following identities apply.

$$\mathbf{D} = \epsilon_r \epsilon_0 \mathbf{E} \quad (1.5)$$

$$\mathbf{B} = \mu_r \mu_0 \mathbf{H} \quad (1.6)$$

$$\mathbf{J} = \sigma \mathbf{E} \quad (1.7)$$

Since PEEC method usually deals with non-magnetic material, μ_r is not of much interest and is taken to be one both for conducting and isolating media.

It is worth, instead, spending few more words on equation 1.5. While permittivity ϵ for dielectrics is a well known topic, explained in almost every physics book, not the same is true when the concept is associated with conductors.

What's the electric permittivity of a good conductor? There is no simple answer. In these media conduction current densities \mathbf{J} are so much larger than displacement current densities $\frac{\partial \mathbf{D}}{\partial t}$, [1].

To show the reason of this, consider a material of conductivity σ and relative permittivity ϵ_r subject to a sinusoidal alternating electric field for which Ampère-Maxwell's equation (1.4) can be written in terms of phasors.

$$\text{curl } \mathbf{H} = j\omega \mathbf{D} + \mathbf{J} \quad (1.8)$$

Given equations 1.6 and 1.7, one can compare amplitudes of the two terms at the right-hand side.

$$\left| \frac{j\omega \mathbf{D}}{\mathbf{J}} \right| = \frac{\omega \epsilon_r \epsilon_0}{\sigma} \quad (1.9)$$

In a good conductor, it may be assumed a conductivity $\sigma \approx 10^7 \frac{\text{S}}{\text{m}}$ and a relative electric permittivity $\epsilon_r \approx 1$, as for ordinary dielectrics, meaning the above ratio is in the order of $\frac{f}{10^{17}}$ at a frequency f .

In conclusion, the contribution of displacement currents is negligible compared with conduction currents, leaving flexibility in choosing the permittivity value of conductors that, for convenience, can be taken equal to the one of the dielectric surrounding them. This assumption shouldn't imply much error for the reason previously detailed, however, the consequences have not been investigated yet.

The environment being shaped, with these choices, is such that it allows the use of the homogeneous space solution for the electric and magnetic potential, explained in the next section.

1.3 Electric scalar and magnetic vector potential wave equations

Usually Maxwell's equations are solved by making use of the electric scalar Φ and magnetic vector potential \mathbf{A} . PEEC represents no difference resorting in its development to the solution of the potentials' wave equations, which will be shortly introduced.

Magnetic Gauss's law (1.2) states that the flux density \mathbf{B} is a divergence free vector field hence there exists a vector potential \mathbf{A} such that

$$\mathbf{B} = \text{curl } \mathbf{A} \quad (1.10)$$

Replacing 1.10 for \mathbf{B} in Faraday's law (1.3) leads to the following.

$$\text{curl} \left(\mathbf{E} + \frac{\partial \mathbf{A}}{\partial t} \right) = 0 \quad (1.11)$$

The term between parentheses is curl free therefore can be written as gradient of a scalar function, the electric scalar potential.

$$-\text{grad } \Phi = \mathbf{E} + \frac{\partial \mathbf{A}}{\partial t} \quad (1.12)$$

To synthesize, equations 1.10 and 1.12 define respectively the magnetic \mathbf{A} and electric potential Φ .

In linear media Ampère's law (1.4) can be rewritten to get

$$\text{curl } \text{curl} \mathbf{A} = \mu \left(\frac{\partial \mathbf{D}}{\partial t} + \mathbf{J} \right) \quad (1.13)$$

which results in 1.14 if equation 1.12 is employed.

$$\text{curl } \text{curl} \mathbf{A} + \mu \epsilon \frac{\partial^2 \mathbf{A}}{\partial t^2} = \mu \mathbf{J} - \mu \epsilon \text{grad} \left(\frac{\partial \Phi}{\partial t} \right) \quad (1.14)$$

Using the vector identity recalled below,

$$\text{curl } \text{curl} \cdot = \text{grad } \text{div} \cdot - \Delta \cdot \quad (1.15)$$

equation 1.14 becomes

$$\Delta \mathbf{A} - \mu\epsilon \frac{\partial^2 \mathbf{A}}{\partial t^2} = -\mu \mathbf{J} + \mu\epsilon \text{grad} \left(\text{div} \mathbf{A} + \frac{\partial \Phi}{\partial t} \right) \quad (1.16)$$

which can be further simplified by considering that the magnetic vector potential is defined with some degree of freedom. Specifically, any vector field whose curl is zero can be added to \mathbf{A} leaving the magnetic flux density unchanged.

Denoting the old magnetic vector potential as \mathbf{A}' , the new magnetic vector potential becomes $\mathbf{A} = \mathbf{A}' + \text{grad} f$, where the arbitrary vector field is expressed as the gradient of a scalar function f , exploiting the fact that it is conservative.

If f is chosen in such a way that

$$\Delta f = -\text{div} \mathbf{A}' - \frac{\partial \Phi}{\partial t} \quad (1.17)$$

or equivalently that

$$\text{div} \mathbf{A} + \frac{\partial \Phi}{\partial t} = 0 \quad (1.18)$$

which is called the Lorenz condition, then equation 1.16 becomes the magnetic vector potential wave equation.

$$\Delta \mathbf{A} - \mu\epsilon \frac{\partial^2 \mathbf{A}}{\partial t^2} = -\mu \mathbf{J} \quad (1.19)$$

Similarly for the electric scalar potential, taking the divergence of equation 1.12 and substituting \mathbf{E} in terms of \mathbf{D} (1.5) leads to

$$\Delta \Phi = -\frac{\text{div} \mathbf{D}}{\epsilon} - \frac{\partial \text{div} \mathbf{A}}{\partial t} \quad (1.20)$$

which can be further simplified by plugging in the electric Gauss's law (1.1) and the Lorenz condition (1.18), obtaining the electric scalar potential wave equation.

$$\Delta \Phi - \frac{\partial^2 \Phi}{\partial t^2} = -\frac{\rho}{\epsilon} \quad (1.21)$$

1.3.1 Solution

In an homogeneous unbounded region V' the solution to the wave equation for the electric potential (1.21) is

$$\Phi = \int_{V'} \int_{t'} \frac{\rho}{\epsilon} g(t - t', \mathbf{r} - \mathbf{r}') dV' dt' \quad (1.22)$$

where g is known as the Green's function, which, in general, is the impulse response of a linear differential equation.

The Green's function for the wave operator is

$$g = \frac{\delta(t - t' - \frac{|\mathbf{r} - \mathbf{r}'|}{\nu})}{|\mathbf{r} - \mathbf{r}'|} \quad (1.23)$$

where $\nu = \frac{1}{\sqrt{\mu\epsilon}}$ is the finite wave speed in the medium, [2].

The expression for the electric potential used in 1.22 is unusual, 1.24 is more common. However, 1.22 is the most explicative if the wave equation is solved through the Green's function approach.

$$\Phi = \int_{V'} \frac{\rho(t - \frac{|\mathbf{r} - \mathbf{r}'|}{\nu})}{4\pi\epsilon|\mathbf{r} - \mathbf{r}'|} dV' \quad (1.24)$$

Finally, the solution for the magnetic vector potential can be found in a similar way on a component per component basis, obtaining

$$\mathbf{A} = \int_{V'} \frac{\mu\mathbf{J}(t - \frac{|\mathbf{r} - \mathbf{r}'|}{\nu})}{4\pi|\mathbf{r} - \mathbf{r}'|} dV' \quad (1.25)$$

1.4 Electric field integral equation

Rewriting equation 1.12 for the electric field \mathbf{E} results in 1.26.

$$\mathbf{E} = -\text{grad } \Phi - \frac{\partial \mathbf{A}}{\partial t} \quad (1.26)$$

This equation has so much importance to deserve a name on its own: Electric Field Integral Equation, EFIE for short. It writes the electric field \mathbf{E} in terms of the scalar and magnetic potential that, as it has been detailed in the previous section, can be expressed as integrals over all the charge and current sources.

1.4.1 EFIE for conducting regions

A less general, but more relevant equation for the development of the PEEC method is the EFIE written for points belonging to a conducting region with contributions to the electric field originating from sources not in the domain under study.

The total electric field is the sum of the scattered electric field, the one generated by the charges and currents defining the scalar and vector potential, and the incident electric field due to external charges or currents.

$$\mathbf{E}_{tot} = \mathbf{E}_{sca} + \mathbf{E}_{inc} \quad (1.27)$$

Equation 1.27 can be developed further by substituting the scattered electric field for the right-hand side member of the EFIE (1.26) and by replacing the total electric field with the constitutive equation 1.7, recalling that 1.28 is being written for a point in a conducting media.

$$\mathbf{E}_{inc} = \frac{\mathbf{J}}{\sigma} + \frac{\partial \mathbf{A}}{\partial t} + \text{grad } \Phi \quad (1.28)$$

1.5 Continuity equation

$$\frac{\partial \rho}{\partial t} + \text{div } \mathbf{J} = 0 \quad (1.29)$$

The continuity equation, expressed in 1.29 with its differential form, states the electric charge conservation. Even though it doesn't add anything to Maxwell's equations, from which could be obtained, it deserves a spot of its own. In fact, together with the EFIE it makes up the set of partial differential equations defining the EM problem.

Chapter 2

Triangular-mesh-based PEEC

PEEC (Partial Element Equivalent Circuit) is a numerical method employed for the approximation of EM (electromagnetic) problems in such a way that casts them into circuit solving problems. The method dates back to 1970s when Albert E. Ruehli working at IBM's Watson research facility in Yorktown Heights, NY, first devised it. His article [3] is widely reported as the pioneering work that gave birth to the method.

PEEC is so called since it deals with equivalent circuits made of circuit elements (inductances, capacitances), which are said to be partial in the way that they are defined for parts (cells) rather than complete conductors.

The first step of the approach is to split the system of conductors into cells, for which equivalent circuits are derived and then arranged together.

Once the equivalent circuit of the whole system is built, the desired electrical responses are obtained via a network analysis program, usually Spice-like circuit simulators [4]; Ngspice [5] is one of them. This type of approach proves effective when the dimension of the problem is small, i.e. there are few cells and weak mutual couplings between them; in all other situations the solution has to be carried out through code written for the purpose.

After so many years PEEC is still an active topic of research and much work needs to be done; proof is that during the writing of this thesis has been published the first book entirely dedicated to PEEC, [6]. The book, written among the others by Ruehli, tries to gather all that has been done in this area and spread across various articles since the early days, helping to introduce more and more people to this rather difficult subject. Before this, only sections of books, as [7], were available.

PEEC started as a numerical method for rectangular geometries, [3]. Only later, it was extended to non-orthogonal, [8], and ultimately to triangular meshes, [9] and [10].

This chapter aims at developing the techniques involving triangles, which

are often preferred because their meshing can be easily automated, i.e. reasonably complicated computer programs can be written to perform the task.

Modelling arbitrarily shaped surfaces with such patches introduces some degree of approximation, however, most of the time, the geometrical variation is so small that can be simply neglected. Furthermore, triangles are widely recognised to conform well to any kind of surface.

2.1 Basis functions

2.1.1 Current basis functions

The current density \mathbf{J} is one of the unknowns of the EM problem and belongs to a space, here referred as V , which collects all the functions \mathbf{v} defined on the conducting structure and satisfying the following boundary condition:

- If $\hat{\mathbf{n}}$ is taken to be the surface normal unit vector then $\mathbf{v} \cdot \hat{\mathbf{n}} = 0$. This is a direct consequence of the charge continuity equation (1.29).

V is an infinite dimension space, therefore finding a solution in it can become quite involved if not impossible. For this reason the possibility of an exact solution is left in favor of an approximate one, sought within a finite dimension sub-space.

The sub-space has to be chosen in such a way that one of its functions can retrace the exact solution as closely as possible. As a result, the next step in the PEEC method is to build an appropriate set of basis functions, whose linear combination can well represent \mathbf{J} . Two possibilities will be explored: RWG and Mackenzie.

RWG basis

For Rao-Wilton-Glisson (RWG), [11], each basis function \mathbf{f}_n is associated with an interior edge and it is null on every triangle except the two neighboring the n th edge.

A space built with such basis automatically satisfies the boundary condition stated at the beginning of the section. This fact can be evinced from its analytical formulation given in 2.1.

$$\mathbf{f}_n(\mathbf{r}) = \begin{cases} \frac{l_n}{2A_n^+} \boldsymbol{\rho}_n^+ & \text{when } \mathbf{r} \text{ is in } T_n^+ \\ \frac{l_n}{2A_n^-} \boldsymbol{\rho}_n^- & \text{when } \mathbf{r} \text{ is in } T_n^- \\ 0 & \text{elsewhere} \end{cases} \quad (2.1)$$

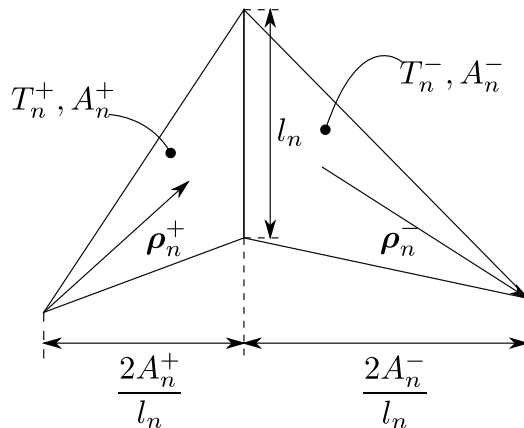


Figure 2.1: Triangle pair and geometrical parameters associated with interior edge.

where T_n^+ and T_n^- are the two triangular patches, A_n^+ and A_n^- their respective areas, l_n the length of the interior edge and $\boldsymbol{\rho}_n^+$ and $\boldsymbol{\rho}_n^-$ are vectors originating or ending in the vertex opposing the common edge, as shown in figure 2.1.

An expression for the current density field can be given as a linear combination of basis functions.

$$\mathbf{J} = \sum_{n=1}^N J_n \mathbf{f}_n \quad (2.2)$$

Since the normal component of \mathbf{f}_n is unitary at the n th edge, each J_n coefficient acquires special meaning, being the uniform current density passing through the edge. To further clarify this statement, equation 2.2 can be rewritten as

$$\mathbf{J} = \sum_{n=1}^N I_n \frac{\mathbf{f}_n}{l_n t} \quad (2.3)$$

highlighting I_n , the current flowing past the n th edge, and t , the thickness of the conducting surface.

For the model to be valid, the thickness needs to be order of magnitude smaller than the triangles' characteristic length.

t has been assumed constant for the whole surface, however nothing prevents from making it a variable of the triangular patch, with the possibility of analysing more general problems.

The use of this basis leads to some limitations in the structures that can be treated. An hypothesis has been implicitly made, when defining the RWG

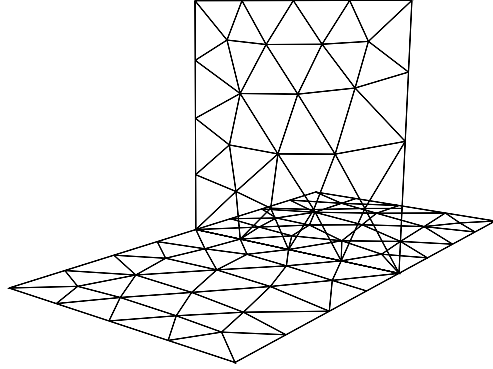


Figure 2.2: T-like structure.

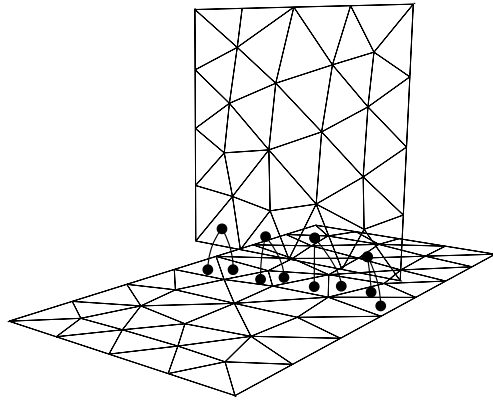


Figure 2.3: Split and joint by ideal shorts T-like structure.

basis, that every edge is attached to no more than two triangles.

The structure represented in figure 2.2 is one of those the approach described so far wouldn't be able to solve. However, there exists a workaround, an example of which is reported in figure 2.3. Here, the surface is cut along the critical edges obtaining two parts that are subsequently connected together through ideal shorts. For clarity purposes, the gap between the two surfaces has been exaggerated, however, it could be made extremely small or even null with proper modelling.

A more general, but surely slower approach is reported in [12], where the basis functions are identical to those presented here except for the fact that they only span a triangle. This substantially doubles the current unknowns but leaves the possibility for properly analysing structures like figure 2.2.

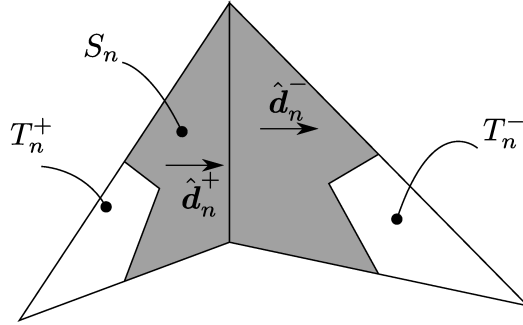


Figure 2.4: Triangle pair and geometrical parameters relevant for Mackenzie's basis functions.

Mackenzie's basis

In [13], a new set of basis functions has been presented, aimed at solving problems where Rao-Wilton-Glisson (RWG) basis functions were generally employed. These simpler functions are defined over pairs of planar triangular patches as well, but have a constant value in the region where they are non null, gaining them also the name of piece-wise constant basis. The function \mathbf{g}_n associated with the n th edge is defined as

$$\mathbf{g}_n(\mathbf{r}) = \begin{cases} \hat{\mathbf{d}}_n^\pm & \text{when } \mathbf{r} \text{ is in } S_n \\ 0 & \text{elsewhere} \end{cases} \quad (2.4)$$

where S_n is the region obtained by connecting the midpoints of the free edges to the nodes of the edge n , and to the centroids of the neighboring triangles. Further, $\hat{\mathbf{d}}_n^\pm$ represent unit vectors laying in the plane of the triangles and perpendicular to the common edge. Figure 2.4 resumes the quantities used above and shows a particular case when $\hat{\mathbf{d}}_n^+$ and $\hat{\mathbf{d}}_n^-$ coincide since both triangles lay in the same plane.

One is now able to write down an expression for the current density as a linear combination of basis functions.

$$\mathbf{J} = \sum_{n=1}^N J_n \mathbf{g}_n \quad (2.5)$$

Equation can be rewritten in a more circuit-friendly way by putting in evidence the total current flowing through the n th edge.

$$\mathbf{J} = \sum_{n=1}^N I_n \frac{\mathbf{g}_n}{l_n t} \quad (2.6)$$

2.1.2 Charge basis functions

The previous subsection has been dedicated to the first unknown of the EM problem; it's time, now, to discuss the second and last one: the charge density ρ , which, in general, belongs to a space, which will be referred as X , of all the scalar functions defined on the conducting domain. In a similar way to what has been done for the current density, a dimension reduction of X is necessary for a numerical solution. The basis for ρ is to be chosen in accordance to the current density in such a way that leaves the possibility to satisfy the continuity equation anywhere in the conducting domain. Although, this leads to a much cleaner approach, standard PEEC does satisfy 1.29 only globally for few determined regions, nevertheless, its effectiveness has been shown several times.

To obtain the basis for the charge density the finite dimension expression of the current density (2.2) is being substituted in the continuity equation.

$$\frac{\partial \rho}{\partial t} = -\operatorname{div} \sum_{n=1}^N J_n \mathbf{f}_n = -\sum_{n=1}^N J_n \operatorname{div} \mathbf{f}_n \quad (2.7)$$

It can be proved (appendix A) that

$$\operatorname{div} \mathbf{f}_n = \begin{cases} \frac{l_n}{A_n^+} & \text{when } \mathbf{r} \text{ is in } T_n^+ \\ -\frac{l_n}{A_n^-} & \text{when } \mathbf{r} \text{ is in } T_n^- \\ 0 & \text{elsewhere} \end{cases} \quad (2.8)$$

These functions are known as pulse doublets, [14].

By integrating equation 2.7 with respect to time, it will be clear the appropriate basis for the charge density.

$$\rho = -\sum_{n=1}^N \operatorname{div} \mathbf{f}_n \int_t J_n dt + Z \quad (2.9)$$

where Z is the constant of integration, a function of the only position.

Selecting $\operatorname{div} \mathbf{f}_n$ as the basis would seem the proper choice, however, by doing so no changes in the total charge of the conducting surfaces would be allowed. This is not strange because, in the continuity equation used for the derivation, the influence of external currents has been totally disregarded.

As a result, since the objective is to model the behaviour of the conducting structure together with other external components that could bring excessive charge on it, a different, larger basis that comprises $\operatorname{div} \mathbf{f}_n$ but adds the possibility of a total charge different from zero is to be adopted. This is the pulse function basis, which describes the space of the piecewise constant

functions. The pulse function u_m is associated with the m th triangle where it takes unitary value and it is zero on every other.

The following equation reports the finite dimension expression of the charge density.

$$\rho = \sum_{m=1}^M \rho_m u_m \quad (2.10)$$

where ρ_m is the value of the uniform electric charge density associated with the m th triangular patch.

In a similar way to the current density, 2.10 can be rewritten to put in evidence the total charge Q_m .

$$\rho = \sum_{m=1}^M Q_m \frac{u_m}{A_m t} \quad (2.11)$$

2.2 Weak formulation of the problem

$$\begin{cases} \mathbf{E}_{inc} = \frac{\mathbf{J}}{\sigma} + \frac{\partial \mathbf{A}}{\partial t} + \text{grad } \Phi \\ 0 = \text{div } \mathbf{J} + \frac{\partial \rho}{\partial t} \end{cases} \quad (2.12)$$

The EM problem, represented by 2.12, can be numerically solved by putting it in its weak formulation (2.13).

$$\begin{cases} \int_S \mathbf{v} \cdot \mathbf{E}_{inc} ds = \int_S \mathbf{v} \cdot \frac{\mathbf{J}}{\sigma} ds + \int_S \mathbf{v} \cdot \frac{\partial \mathbf{A}}{\partial t} ds + \int_S \mathbf{v} \cdot \text{grad } \Phi ds \\ 0 = \int_S x \frac{\partial \rho}{\partial t} ds + \int_S x \text{div } \mathbf{J} ds \end{cases} \quad (2.13)$$

2.13 is to be verified for any function \mathbf{v} in V , the infinite dimension space of the current density, and for any x in X , the infinite dimension space of the charge density.

The procedure linking equation 2.12 to 2.13 is known as testing while \mathbf{v} and x , the kernels of the integrals, are known as test functions.

From now on the focus will be on the weak formulation of the EFIE that can be further developed using the vector calculus identity $\text{div}(\Phi \mathbf{v}) = \text{div } \mathbf{v} \Phi + \mathbf{v} \cdot \text{grad } \Phi$, leading to

$$\int_S \mathbf{v} \cdot \mathbf{E}_{inc} ds = \int_S \mathbf{v} \cdot \frac{\mathbf{J}}{\sigma} ds + \int_S \mathbf{v} \cdot \frac{\partial \mathbf{A}}{\partial t} ds - \int_S \operatorname{div} \mathbf{v} \Phi ds + \int_S \operatorname{div} (\Phi \mathbf{v}) ds \quad (2.14)$$

Green's theorem can be applied to the last term obtaining $\int_{\partial S} \Phi \mathbf{v} \cdot \hat{\mathbf{n}} dl$, that is recognised to be null since $\mathbf{v} \cdot \hat{\mathbf{n}} = 0$ on the boundary, reducing 2.14 to 2.15.

$$\int_S \mathbf{v} \cdot \mathbf{E}_{inc} ds = \int_S \mathbf{v} \cdot \frac{\mathbf{J}}{\sigma} ds + \int_S \mathbf{v} \cdot \frac{\partial \mathbf{A}}{\partial t} ds - \int_S \operatorname{div} \mathbf{v} \Phi ds \quad (2.15)$$

The following will be limited to the derivation of the quasi-static PEEC for the sake of simplicity, although a full-wave formulation could be obtained in a similar way. Quasi-static PEEC means neglecting the time retardation in the integral formulation of the potentials, equations 1.24 and 1.25. This can be done correctly when the wavelength of the highest frequency in the excitation is much longer than the characteristic dimension of the structure, [15]. The vector magnetic and scalar electric potentials appearing in 2.15 can be expressed in terms of current and charge sources, using the non retarded expressions.

$$\begin{aligned} \int_S \mathbf{v} \cdot \mathbf{E}_{inc} ds = & \frac{1}{\sigma} \int_S \mathbf{v} \cdot \mathbf{J} ds + \\ & \frac{\mu t}{4\pi} \frac{\partial}{\partial t} \int_S \mathbf{v} \cdot \int_S \frac{\mathbf{J}}{|\mathbf{r} - \mathbf{r}'|} ds' ds - \\ & \frac{t}{4\pi\epsilon} \int_S \operatorname{div} \mathbf{v} \int_S \frac{\rho}{|\mathbf{r} - \mathbf{r}'|} ds' ds \end{aligned} \quad (2.16)$$

2.3 Problem discretization

During decades of numerical analysis many discretization approaches have been devised and proved effective. They translate the solution of a set of partial differential equations into a system of linear equations. This section focuses on:

- Galärkin approach
- Collocation approach

differing for the testing procedure employed. The interested reader can refer to [16] for a more complete list of techniques.

So far no substantial approximation has been done, in fact, the weak formulation has just been an analytical elaboration of the starting problem. However, in order to pursue a numerical solution it becomes necessary to do a big one, that is reducing the space dimension of the test and solution functions.

2.3.1 Galärkin approach

In this section, the Galärkin approach will be applied to the EFIE leaving for the continuity equation only the final result. The first step is reducing the dimensions of the spaces for the charge and current density, employing the basis already developed.

$$\begin{aligned}
\int_S \mathbf{v} \cdot \mathbf{E}_{inc} ds &= \frac{1}{\sigma t} \sum_{k=1}^N I_k \int_S \frac{\mathbf{f} \cdot \mathbf{f}_k}{l_k} ds + \\
&\frac{\mu}{4\pi t} \sum_{k=1}^N \frac{\partial I_k}{\partial t} \int_S \mathbf{v} \cdot \int_S \frac{\mathbf{f}_k}{l_k |\mathbf{r} - \mathbf{r}'|} ds' ds - \\
&\frac{1}{4\pi \epsilon t} \sum_{k=1}^M Q_k \int_S \operatorname{div} \mathbf{v} \int_{T_k} \frac{1}{A_k |\mathbf{r} - \mathbf{r}'|} ds' ds \quad (2.17)
\end{aligned}$$

The Galärkin method is widely recognized for using as test functions the same functions for the expansion of the scalar and vector unknowns. This allows to break down 2.17 in an equivalent set of equations, as many as the number of interior edges N .

$$\begin{aligned}
\frac{1}{l_n} \int_S \mathbf{f}_n \cdot \mathbf{E}_{inc} ds &= \frac{1}{\sigma l_n t} \sum_{k=1}^N I_k \int_S \frac{\mathbf{f}_n \cdot \mathbf{f}_k}{l_k} ds + \\
&\frac{\mu}{4\pi l_n} \sum_{k=1}^N \frac{\partial I_k}{\partial t} \int_S \mathbf{f}_n \cdot \int_S \frac{\mathbf{f}_k}{l_k |\mathbf{r} - \mathbf{r}'|} ds' ds - \\
&\frac{1}{4\pi \epsilon A_n^+} \sum_{k=1}^M Q_k \int_{T_n^+} \int_{T_k} \frac{1}{A_k |\mathbf{r} - \mathbf{r}'|} ds' ds + \\
&\frac{1}{4\pi \epsilon A_n^-} \sum_{k=1}^M Q_k \int_{T_n^-} \int_{T_k} \frac{1}{A_k |\mathbf{r} - \mathbf{r}'|} ds' ds \quad (2.18) \\
&\forall n \in N
\end{aligned}$$

Each of the equations 2.18 can be rewritten in a more compact form by lumping the integrals into parameters.

$$V_n^{inc} = \sum_{k=1}^N I_k R p_{nk} + \sum_{k=1}^N \frac{\partial I_k}{\partial t} L p_{nk} - \sum_{k=1}^M Q_k P p_{n+k} + \sum_{k=1}^M Q_k P p_{n-k} \quad (2.19)$$

Equation 2.19 is susceptible of a circuit interpretation. The Rp terms are nothing more than resistances. Lps are one self and several mutual inductances. Pps are known as coefficients of potential (capacitive terms) while the left-hand side member is a voltage source. It can be proved that only five out of N resistive terms are non null, they could be even less if some of the edges belonging to the two triangles with the n th edge in common are of the boundary kind.

The whole equation 2.19 can be thought as a Kirchhoff's voltage law for a network's branch. As it's known from basic electrical engineering, in order to solve a circuit both Kirchhoff's voltage and current laws need to be written, therefore one more set of equations is to be obtained. Inside the framework of the Galérkin approach, this is done by testing the continuity equation (1.29) against the pulse functions. In practice, it suffices to write the conservation of the electric charge for every triangular patch.

$$\frac{\partial Q_m}{\partial t} = \sum_{k=1}^3 \pm I_k \quad \forall m \in M \quad (2.20)$$

where the I_k is to be taken positive or negative depending on the direction of the conventional current, that could be flowing in or out of the triangle.

Similarly to 2.19, 2.20 can be interpreted as Kirchhoff's current laws for network's nodes.

PEEC implementing Galérkin method is immediately recognizable for having symmetric mutual couplings between partial elements, $Lp_{kn} = Lp_{nk}$ and $Pp_{km} = Pp_{mk}$, leading to some major results.

Let's suppose to deal with a problem whose magnetic coupling is described by an $n \times n$ matrix, then only $\frac{n(n+1)}{2}$ elements need computation with savings in terms of both time and memory. The same argument can be repeated for the coefficients of potential.

Another major result regards the equivalent circuit, which could be drawn out of the parameters using only passives (resistances, capacitances, inductances and transformers), avoiding controlled sources. This is intuitively satisfying in the possibility of representing a passive physical system with passive electrical components.

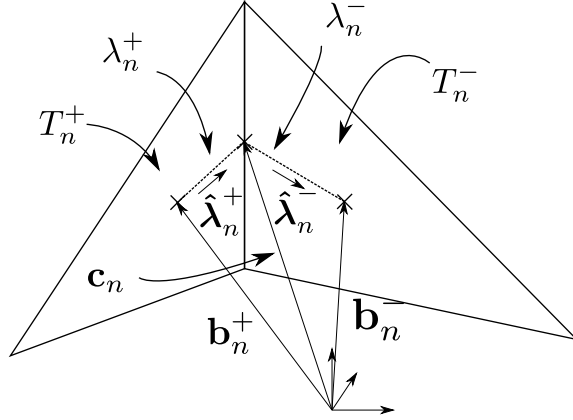


Figure 2.5: Collocation approach: current test function.

2.3.2 Collocation approach

Standard PEEC has customary been based on the Gal rkin approach and on the symmetry of circuit elements, [6]. The same is true for those based on triangular meshes, [9] and [10], that, however, have also witnessed other solutions. For instance, in [17] a different choice for the test functions is done. In particular for the EFIE, test functions are chosen in a space W , a sub-space of V , whose basis is formed by the functions \mathbf{w}_n in 2.21, one for each interior edge.

$$\mathbf{w}_n(\mathbf{r}) = \begin{cases} \hat{\boldsymbol{\lambda}}_n^+ & \text{when } \mathbf{r} \text{ belongs to } \lambda_n^+ \\ \hat{\boldsymbol{\lambda}}_n^- & \text{when } \mathbf{r} \text{ belongs to } \lambda_n^- \\ 0 & \text{elsewhere} \end{cases} \quad (2.21)$$

where λ_n^+ and λ_n^- denote the segments connecting the midpoint of the edge n to the centroids of the two neighboring triangles, T_n^+ and T_n^- respectively, while $\hat{\boldsymbol{\lambda}}_n^+$ and $\hat{\boldsymbol{\lambda}}_n^-$ are unit vectors directed along the λ_n^+ and λ_n^- segments pointing towards or away from the midpoint as shown in figure 2.5.

The expansion functions for the unknowns remain those developed at the beginning of the chapter. Therefore, the collocation approach starts differing from Gal rkin only in equation 2.17, when the test function space is reduced into W , leading to the following:

$$\int_S \mathbf{w}_n \cdot \mathbf{E}_{inc} ds = \int_S \mathbf{w}_n \cdot \frac{\mathbf{J}}{\sigma} ds + \frac{\partial}{\partial t} \int_S \mathbf{w}_n \cdot \mathbf{A} ds - \int_S \Phi \operatorname{div} \mathbf{w}_n ds \quad (2.22)$$

$\forall n \in N$

The next step is to find an expression for $\text{div } \mathbf{w}_n$, which is of straightforward evaluation.

$$\text{div } \mathbf{w}_n(\mathbf{r}) = \delta(\mathbf{r} - \mathbf{b}_n^+) - \delta(\mathbf{r} - \mathbf{b}_n^-) \quad (2.23)$$

At this point it becomes necessary to plug in the discretized expressions for the current and charge density. Several choices are available substantially differing for the current expansion, in the following the development will be limited to RWG and Mackenzie's basis.

RWG basis

Introducing the discretized expressions for the sources in the set of equations 2.22 gets

$$\begin{aligned} \int_{\lambda_n} \hat{\boldsymbol{\lambda}}_n \cdot \mathbf{E}_{inc} dl &= \frac{1}{t\sigma} \sum_{k=1}^N I_k \int_{\lambda_n} \frac{\hat{\boldsymbol{\lambda}}_n \cdot \mathbf{f}_k}{l_k} dl + \\ &\frac{\mu}{4\pi} \sum_{k=1}^N \frac{\partial I_k}{\partial t} \int_{\lambda_n} \hat{\boldsymbol{\lambda}}_n \cdot \int_S \frac{\mathbf{f}_k}{l_k |\mathbf{r} - \mathbf{r}'|} ds' dl - \\ &\frac{1}{4\pi\epsilon} \sum_{k=1}^M Q_k \int_{T_k} \frac{1}{A_k |\mathbf{b}_n^+ - \mathbf{r}'|} ds' + \\ &\frac{1}{4\pi\epsilon} \sum_{k=1}^M Q_k \int_{T_k} \frac{1}{A_k |\mathbf{b}_n^- - \mathbf{r}'|} ds' \end{aligned} \quad (2.24)$$

$\forall n \in N$

Each of the equations 2.24 can be rewritten in a more compact form by lumping the integrals into parameters.

$$V_n^{inc} = \sum_{k=1}^N I_k R p_{nk} + \sum_{k=1}^N \frac{\partial I_k}{\partial t} L p_{nk} - \sum_{k=1}^M Q_k P p_{n+k} + \sum_{k=1}^M Q_k P p_{n-k} \quad (2.25)$$

As can be seen equation 2.25 is formally identical to equation 2.19, the only difference hides in the expression of the parameters, which result greatly simplified. The easiness of computation, deriving from it, doesn't come for free. In fact, the inductive and capacitive terms are not symmetric anymore, meaning that in principle all the entries of the coupling matrices need to be computed.

As it was for the Galérkin approach, a set of equations is still missing. However, this time, as opposed to before, it will be derived by passing through the rigorous testing of the continuity equation (1.29) against the pulse functions u_m .

$$\int_S u_m \frac{\partial \rho}{\partial t} ds = - \int_S u_m \operatorname{div} \mathbf{J} ds \quad \forall m \in M \quad (2.26)$$

Applying Green's theorem to the second member of equation 2.26 and plugging in the expression for the charge density at the first member, the same equation as the Galérkin approach is obtained (2.20).

$$\frac{\partial Q_m}{\partial t} = \sum_{k=1}^3 \pm I_k \quad \forall m \in M \quad (2.27)$$

Mackenzie's basis

Introducing the discretized expressions for the sources in the set of equations 2.22 leads to:

$$\begin{aligned} \int_{\lambda_n} \hat{\boldsymbol{\lambda}}_n \cdot \mathbf{E}_{inc} dl &= \frac{1}{w\sigma} \sum_{k=1}^N I_k \int_{\lambda_n} \frac{\hat{\boldsymbol{\lambda}}_n \cdot \mathbf{g}_k}{l_k} dl + \\ &\frac{\mu}{4\pi} \sum_{k=1}^N \frac{\partial I_k}{\partial t} \int_{\lambda_n} \hat{\boldsymbol{\lambda}}_n \cdot \int_S \frac{\mathbf{g}_k}{l_k |\mathbf{r} - \mathbf{r}'|} ds' dl - \\ &\frac{1}{4\pi\epsilon} \sum_{k=1}^M Q_k \int_{T_k} \frac{1}{A_k |\mathbf{b}_n^+ - \mathbf{r}'|} ds' + \\ &\frac{1}{4\pi\epsilon} \sum_{k=1}^M Q_k \int_{T_k} \frac{1}{A_k |\mathbf{b}_n^- - \mathbf{r}'|} ds' \end{aligned} \quad (2.28)$$

$\forall n \in N$

and by hiding the integrals behind new parameters, equation 2.25 is obtained.

The testing of the electric charge conservation law won't be detailed, suffice it to say, it leads to the same equation 2.27, already found for RWG.

2.4 Equivalent circuit

As it has been seen, both the pursued approaches, Galérkin and collocation, lead to the same branch (2.19, 2.25) and node-like equations (2.20, 2.27)

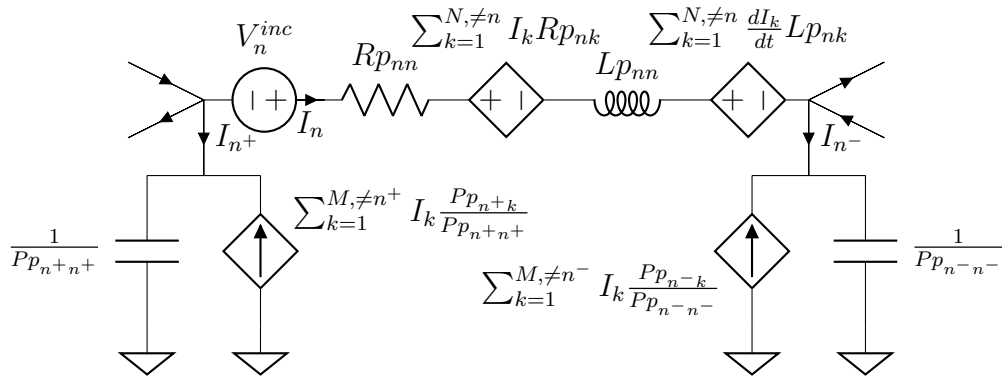


Figure 2.6: Elementary cell of PEEC model.

from which an equivalent circuit can be built. In figure 2.6 one of the many elementary cells that form the equivalent circuit is being presented.

Chapter 3

Evaluation of circuit elements

This chapter goes through the formulae for the circuit element parameters, which are almost as-is implemented in the developed PEEC library.

The focus is on the collocation approach. The Galérkin one, of which basic principles have been previously given, will be left behind.

3.1 Partial resistances

$$Rp_{nk} = \begin{cases} \frac{1}{t\sigma} \int_{\lambda_n} \frac{\hat{\lambda}_n \cdot \mathbf{f}_k}{l_k} dl & \text{for RWG} \\ \frac{1}{t\sigma} \int_{\lambda_n} \frac{\hat{\lambda}_n \cdot \mathbf{g}_k}{l_k} dl & \text{for Mackenzie} \end{cases} \quad (3.1)$$

These represent general formulations for both current basis functions. For Mackenzie's, only self terms are non-null, while for RWG, even mutual terms are possible. For these latter case, efficient computation can be reached by developing two formulae, one for each term (self and mutual).

3.1.1 Self term

RWG basis

$$Rp_{nn} = \frac{1}{t\sigma} \int_{\lambda_n} \frac{\hat{\lambda}_n \cdot \mathbf{f}_n}{l_n} dl \quad (3.2)$$

The n th self partial resistance is computed by splitting the line integral over the two triangles neighboring the n th edge and by plugging in the expression for \mathbf{f}_n .

$$Rp_{nn} = \frac{1}{2t\sigma A_n^+} \int_{\lambda_n^+} \hat{\lambda}_n^+ \cdot \boldsymbol{\rho}_n^+ dl + \frac{1}{2t\sigma A_n^-} \int_{\lambda_n^-} \hat{\lambda}_n^- \cdot \boldsymbol{\rho}_n^- dl \quad (3.3)$$

By noticing that $\boldsymbol{\rho}_n^\pm$ and $\hat{\lambda}_n^\pm$ are parallel on the integration domain:

$$Rp_{nn} = \frac{1}{2t\sigma A_n^+} \int_{\lambda_n^+} \rho_n^+ dl + \frac{1}{2t\sigma A_n^-} \int_{\lambda_n^-} \rho_n^- dl \quad (3.4)$$

ρ_n^+ and ρ_n^- are linear functions, therefore computing the integrals becomes a simple matter of taking the product of the line integral length times the average of the extreme values, leading to:

$$Rp_{nn} = \frac{1}{2t\sigma A_n^+} \lambda_n^+ \frac{\rho_n^+(\mathbf{b}_n^+) + \rho_n^+(\mathbf{c}_n)}{2} + \frac{1}{2t\sigma A_n^-} \lambda_n^- \frac{\rho_n^-(\mathbf{b}_n^-) + \rho_n^-(\mathbf{c}_n)}{2} \quad (3.5)$$

where \mathbf{c}_n is the midpoint of the n th edge. See figure 2.5 for details about notation.

Still, this is susceptible of simplification, in fact, in a triangle the median crosses the barycenter at exactly two third of its length. Property that can be leveraged to write 3.6.

$$Rp_{nn} = \frac{5}{4t\sigma} \left(\frac{\lambda_n^{+2}}{A_n^+} + \frac{\lambda_n^{-2}}{A_n^-} \right) \quad (3.6)$$

Mackenzie's basis

$$Rp_{nn} = \frac{1}{t\sigma} \int_{\lambda_n} \frac{\hat{\boldsymbol{\lambda}}_n \cdot \mathbf{g}_n}{l_n} dl \quad (3.7)$$

The n th self partial resistance is computed by splitting the line integral over the two triangles neighboring the n th edge and plugging in the expression for \mathbf{g}_n .

$$Rp_{nn} = \frac{1}{t\sigma} \int_{\lambda_n^+} \frac{\hat{\boldsymbol{\lambda}}_n^+ \cdot \hat{\mathbf{d}}_n^+}{l_n} dl + \frac{1}{t\sigma} \int_{\lambda_n^-} \frac{\hat{\boldsymbol{\lambda}}_n^- \cdot \hat{\mathbf{d}}_n^-}{l_n} dl \quad (3.8)$$

Simplifying a tad, a formula directly usable in coding is obtained.

$$Rp_{nn} = \frac{1}{t\sigma} \frac{\boldsymbol{\lambda}_n^+ \cdot \hat{\mathbf{d}}_n^+ + \boldsymbol{\lambda}_n^- \cdot \hat{\mathbf{d}}_n^-}{l_n} = \frac{1}{t\sigma} \frac{|\boldsymbol{\lambda}_n^+ \times \mathbf{l}_n| + |\boldsymbol{\lambda}_n^- \times \mathbf{l}_n|}{l_n^2} \quad (3.9)$$

3.1.2 Mutual term

RWG basis

Each branch identified by an interior edge is subject to at most four mutual resistive couplings, one for each edge (not the common) of its neighboring triangles.

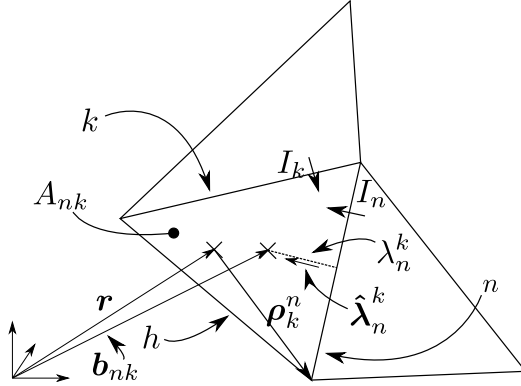


Figure 3.1: Geometry for resistive mutual term evaluation.

$$Rp_{nk} = \frac{1}{t\sigma} \int_{\lambda_n} \frac{\hat{\lambda}_n \cdot \mathbf{f}_k}{l_k} dl \quad (3.10)$$

n th edge mutual terms involve integration over only one of the two triangles attached to it. In particular, it is the triangle surrounded by edges n and k , if k labels the edge source of the coupling. Therefore, a first reduction is easily achieved restricting the domain of integration.

$$Rp_{nk} = \frac{1}{2t\sigma A_{nk}} \int_{\lambda_n^k} \hat{\lambda}_n^k \cdot \boldsymbol{\rho}_k^n dl \quad (3.11)$$

where λ_n^k is the part of λ_n pertaining to the triangular patch surrounded by edge n and k , see figure 3.1 for the adopted notation.

To carry on the development, it's necessary a mathematical description for $\boldsymbol{\rho}_k^n$ in terms of more manageable functions, found in [17], here below reported.

$$\boldsymbol{\rho}_k^n(\mathbf{r}) = \boldsymbol{\rho}_k^n(\mathbf{r}_h)N_h(\mathbf{r}) + \boldsymbol{\rho}_k^n(\mathbf{r}_n)N_n(\mathbf{r}) \quad (3.12)$$

where h denotes the third and last edge forming the interested triangle, together with n and k , while N s are nodal functions (also known as tent, rooftop functions), so called since their value is one in the subscripted node and zero on every other, linearly varying in between. The nodes are named according to the edge opposing them, see figure 3.2 for the indexing of the vertices and an example of nodal function.

The next step is to replace equation 3.12 into Rp_{nk} , obtaining:

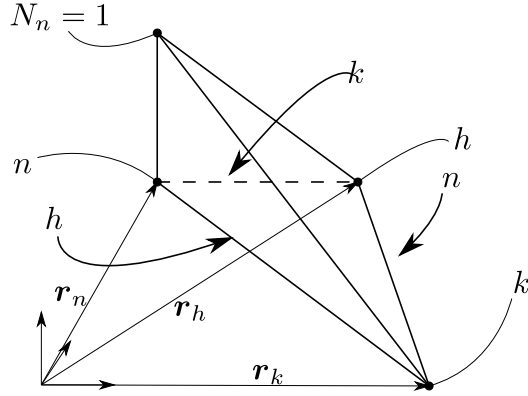


Figure 3.2: Nodal (tent, rooftop) function.

$$Rp_{nk} = \frac{1}{2t\sigma A_{nk}} \left(\hat{\lambda}_n^k \cdot \rho_k^n(\mathbf{r}_h) \int_{\lambda_n^k} N_h(\mathbf{r}) dl + \hat{\lambda}_n^k \cdot \rho_k^n(\mathbf{r}_n) \int_{\lambda_n^k} N_n(\mathbf{r}) dl \right) \quad (3.13)$$

Finally, in a similar way as did in the previous subsection 3.1.1, the integrals, being linear, are trivial and can be computed exploiting the properties for the barycenter of a triangle.

$$Rp_{nk} = \frac{\lambda_n^k}{12t\sigma A_{nk}} \cdot \left(\frac{5}{2} \rho_k^n(\mathbf{r}_h) + \rho_k^n(\mathbf{r}_n) \right) \quad (3.14)$$

3.2 Integrals of the Laplace operator Green's function times linear functions on polygonal domains

In this section the problem of integrating the Laplace operator Green's function times linear functions on a plane triangle is addressed. It should be clear that the solution of this problem allows one to obtain results also for polygonal domains, which will be briefly addressed at the end of the discussion. This study results propaedeutic for the successive development of capacitive and inductive parameters.

Several articles have been written on the topic, for example [18] and [19]. In [19], an integer numbering of the nodes is put in place and the computation of integrals having as kernel $\frac{1}{|\mathbf{r}_0 - \mathbf{r}'|}$ is performed in a local reference frame (u, v, w) , identified as follows:

- Node 1 is the origin of the reference frame.
- The u axis passes through node 2.
- The triangle lays in the uv plane

The article reports the following results:

$$\mathbf{I}_{\mathcal{N}}(T, \mathbf{r}_0) = \begin{bmatrix} I_{N_1} \\ I_{N_2} \\ I_{N_3} \end{bmatrix} = \int_T \begin{bmatrix} N_1 \\ N_2 \\ N_3 \end{bmatrix} \frac{1}{|\mathbf{r}_0 - \mathbf{r}'|} ds' = \begin{bmatrix} 1 & -1 & \left(\frac{u_3}{l_3} - 1\right) \\ 0 & 1 & -\frac{u_3}{l_3} \\ 0 & 0 & 1 \end{bmatrix} \begin{bmatrix} I_1 \\ I_{u_a} \\ I_{v_a} \\ v_3 \end{bmatrix} \quad (3.15)$$

$$I_1(T, \mathbf{r}_0) = \int_T \frac{1}{|\mathbf{r}_0 - \mathbf{r}'|} ds' = -|w_0|\beta + \sum_{i=1}^3 t_i^0 f_{2i} \quad (3.16)$$

where,

$$\begin{bmatrix} I_u \\ I_v \end{bmatrix} = \begin{bmatrix} u_0 \\ v_0 \end{bmatrix} I_1 + \begin{bmatrix} I_{u_a} \\ I_{v_a} \end{bmatrix} \quad (3.17)$$

$$\begin{bmatrix} I_{u_a} \\ I_{v_a} \end{bmatrix} = \frac{1}{2} \begin{bmatrix} \hat{\mathbf{u}} \\ \hat{\mathbf{v}} \end{bmatrix} \cdot \sum_{i=1}^3 \hat{\mathbf{m}}_i f_{3i} \quad (3.18)$$

$$f_{3i} = (s_i^+ R_i^+ - s_i^- R_i^-) + (R_i^0)^2 f_{2i} \quad (3.19)$$

$$f_{2i} = \ln \left(\frac{R_i^+ + s_i^+}{R_i^- + s_i^-} \right) \quad (3.20)$$

$$\beta = \sum_{i=1}^3 \beta_i \quad (3.21)$$

with,

$$\beta_i = \tan^{-1} \frac{t_i^0 s_i^+}{(R_i^0)^2 + |w_0| R_i^+} - \tan^{-1} \frac{t_i^0 s_i^-}{(R_i^0)^2 + |w_0| R_i^-} \quad (3.22)$$

Lots of symbols have been introduced, hence an explanation is required. u , v and w identify coordinates in the local reference frame. l_3 is the length of the third edge. $\hat{\mathbf{u}}$, $\hat{\mathbf{v}}$ and $\hat{\mathbf{m}}_i$ are all unit vectors. While the meaning of

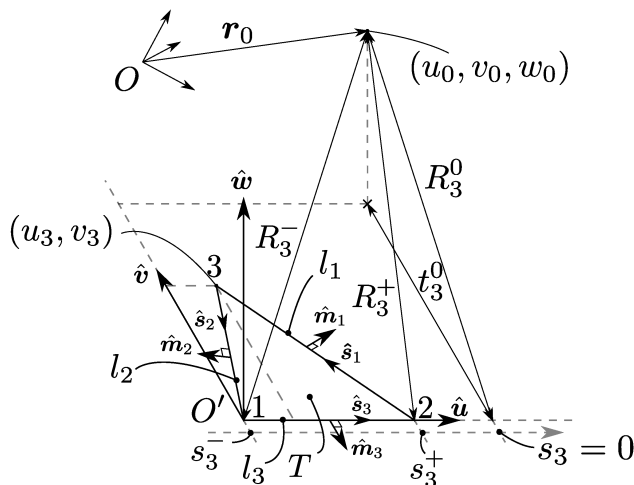


Figure 3.3: Geometry for the evaluation of the Laplace operator Green's function times a linear function integral.

$\hat{\mathbf{u}}$ and $\hat{\mathbf{v}}$ is pretty obvious, not obvious is that of $\hat{\mathbf{m}}_i$, which are unit vectors normal to the edges of the triangle, laying in its plane and outward pointing. R and t terms are distances, respectively from the observation point and from its projection in the plane. Finally, s terms are coordinates identifying points along the edges or their extensions. Their sign does matter, therefore it's important to specify that their zero correspond to the projection of the observation point on the edge and they grow from the lower indexed node to the higher. See figure 3.3 for a more comprehensive view of the quantities at stake.

To this point only triangles have been considered, nevertheless obtaining expressions for other geometries can become relevant in some situations. Luckily, complex polygons can be thought as a compound of triangles. Different subdivisions are possible, however some are preferred, leading to the minimum amount of triangles. As a side note, it's worth specifying that there even exist formulae, like those reported in [18], that are directly applicable to arbitrary polygons.

Let's take, as an example, the pentagon of figure 3.4 for which it is required to compute the integral of the Laplace operator Green's function, result that will return handy in the development of partial inductances for Mackenzie's basis. This pentagon is such well-behaved that only two triangles are sufficient to break it down, therefore:

$$I_1(S, \mathbf{r}_0) = \int_S \frac{1}{|\mathbf{r}_0 - \mathbf{r}'|} ds' = I_1(S_1, \mathbf{r}_0) + I_1(S_2, \mathbf{r}_0) \quad (3.23)$$

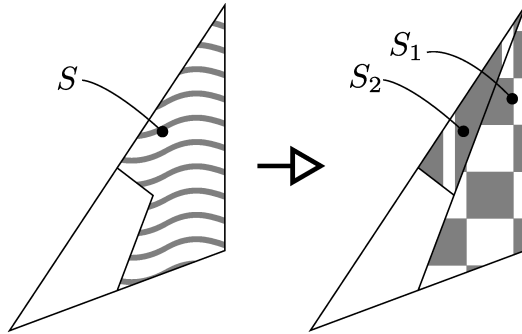


Figure 3.4: Typical Mackenzie's pentagonal shape splitting

3.3 Partial coefficients of potential

In partial coefficients of potential, mutual and self terms can be treated indifferently.

$$Pp_{mk} = \frac{1}{4\pi\epsilon A_k} \int_{T_k} \frac{1}{|\mathbf{b}_m - \mathbf{r}'|} ds' \quad (3.24)$$

Their evaluation is quite involved for the presence of the integral which cannot be solved through simple rules such as those applied for partial resistances. However, there is no need to resort to numerical integration with great savings in terms of computational time, in fact, an analytical expression has purposely been given in the previous section. Equation 3.16 can be directly employed in 3.24, obtaining for the partial coefficients of potential formula 3.25.

$$Pp_{mk} = \frac{I_1(T_k, \mathbf{b}_m)}{4\pi\epsilon A_k} \quad (3.25)$$

3.4 Partial inductances

$$Lp_{nk} = \begin{cases} \frac{\mu}{4\pi l_k} \int_{\lambda_n} \hat{\boldsymbol{\lambda}}_n \cdot \int_S \frac{\mathbf{f}_k}{|\mathbf{r} - \mathbf{r}'|} ds' dl & \text{for RWG} \\ \frac{\mu}{4\pi l_k} \int_{\lambda_n} \hat{\boldsymbol{\lambda}}_n \cdot \int_S \frac{\mathbf{g}_k}{|\mathbf{r} - \mathbf{r}'|} ds' dl & \text{for Mackenzie} \end{cases} \quad (3.26)$$

Partial inductances have no closed form expression, in fact, an analytical solution to the double folded integrals appearing in 3.26 is yet to be found, therefore, an approximation is very much needed. The approach is to evaluate numerically the external integral exploiting the solution of the internal one, which can be found in scientific literature, and has been given in the dedicated section.

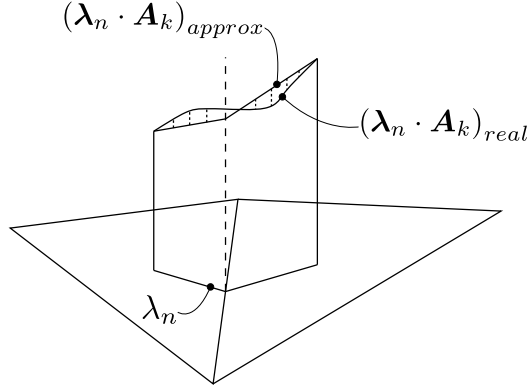


Figure 3.5: Trapezoidal approximation.

Note that RWG and Mackenzie expressions appearing in 3.26 can be synthesized as:

$$Lp_{nk} = \int_{\lambda_n} \hat{\lambda}_n \cdot \mathbf{A}_k(\mathbf{r}) dl \quad (3.27)$$

where $\mathbf{A}_k(\mathbf{r})$ is the magnetic vector potential at a point \mathbf{r} due to a unitary current passing through the k th edge.

This notation is convenient in the way that peculiarities between the two approaches are being hidden behind this term, and the issue of numerical approximation can be dealt with indifferently.

3.4.1 Line integral approximation

Several approaches are available for the approximation of a line integral, they differ for the amount of error committed but all are valid alternatives. Typically, a large number of points Gaussian quadrature rule is employed. This procedure can become computationally expensive, therefore, since this thesis is all about optimization and speed, a simpler two-point trapezoidal rule has been preferred.

$$Lp_{nk} = (\lambda_n^+ + \lambda_n^-) \frac{\hat{\lambda}_n^+ \cdot \mathbf{A}_k(\mathbf{b}_n^+) + \hat{\lambda}_n^- \cdot \mathbf{A}_k(\mathbf{b}_n^-)}{2} \quad (3.28)$$

An even simpler rectangular approximation is also made available through the developed library, which has been verified to return a cleaner code flow.

$$Lp_{nk} = \lambda_n^+ \cdot \mathbf{A}_k(\mathbf{b}_n^+) + \lambda_n^- \cdot \mathbf{A}_k(\mathbf{b}_n^-) \quad (3.29)$$

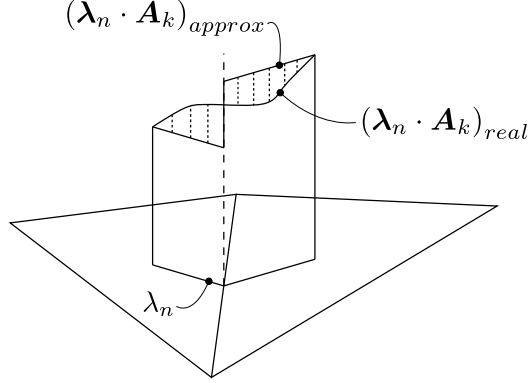


Figure 3.6: Rectangular approximation.

3.4.2 Magnetic vector potential due to unitary edge current

Approximated the line integral, one last thing is left to do, that's find an analytical expression for the magnetic vector potential at a point due to a unitary current flowing past an interior edge.

RWG basis

$$\mathbf{A}_k(\mathbf{r}) = \frac{\mu}{4\pi l_k} \int_S \frac{\mathbf{f}_k}{|\mathbf{r} - \mathbf{r}'|} ds' \quad (3.30)$$

As a starter, the surface integral in 3.30 is reduced and split over the triangles neighboring the k th edge.

$$\mathbf{A}_k(\mathbf{r}) = \frac{\mu}{8\pi} \left(\frac{1}{A_k^+} \int_{T_k^+} \frac{\boldsymbol{\rho}_k^+}{|\mathbf{r} - \mathbf{r}'|} ds' + \frac{1}{A_k^-} \int_{T_k^-} \frac{\boldsymbol{\rho}_k^-}{|\mathbf{r} - \mathbf{r}'|} ds' \right) \quad (3.31)$$

3.31 is developed by breaking down $\boldsymbol{\rho}_k^+$ and $\boldsymbol{\rho}_k^-$ in terms of simpler functions using identity 3.12, already exploited in the section dedicated to partial resistances.

$$\mathbf{A}_k(\mathbf{r}) = \frac{\mu}{8\pi} \left[\frac{1}{A_k^+} \left(\boldsymbol{\rho}_k^+(\mathbf{r}_h^+) \int_{T_k^+} \frac{N_h^+}{|\mathbf{r} - \mathbf{r}'|} ds' + \boldsymbol{\rho}_k^+(\mathbf{r}_j^+) \int_{T_k^+} \frac{N_j^+}{|\mathbf{r} - \mathbf{r}'|} ds' \right) + \frac{1}{A_k^-} \left(\boldsymbol{\rho}_k^-(\mathbf{r}_h^+) \int_{T_k^-} \frac{N_h^-}{|\mathbf{r} - \mathbf{r}'|} ds' + \boldsymbol{\rho}_k^-(\mathbf{r}_j^+) \int_{T_k^-} \frac{N_j^-}{|\mathbf{r} - \mathbf{r}'|} ds' \right) \right] \quad (3.32)$$

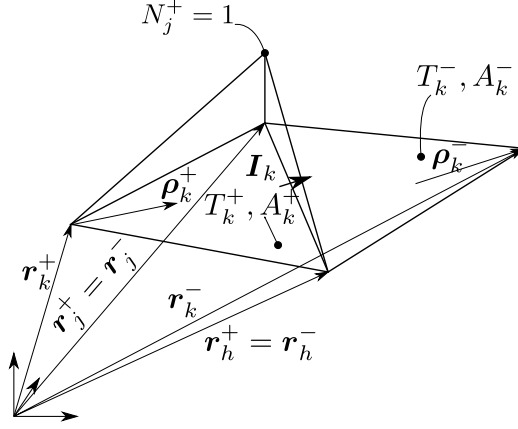


Figure 3.7: Geometry for RWG magnetic vector potential evaluation.

Equation 3.32 is full of notation, that although heavy, results necessary, figure 3.7 is an attempt to be a quick reference for the corresponding geometry.

The solution of integrals appearing 3.32 have been already tackled in the dedicated section, therefore it's now just a matter of using those results to write 3.33, directly computer programmable.

$$\mathbf{A}_k(\mathbf{r}) = \frac{\mu}{8\pi} \left[\frac{1}{A_k^+} (\boldsymbol{\rho}_k^+(\mathbf{r}_h^+) I_{N_h}(T_k^+, \mathbf{r}) + \boldsymbol{\rho}_k^+(\mathbf{r}_j^+) I_{N_j}(T_k^+, \mathbf{r})) + \frac{1}{A_k^-} (\boldsymbol{\rho}_k^-(\mathbf{r}_h^-) I_{N_h}(T_k^-, \mathbf{r}) + \boldsymbol{\rho}_k^-(\mathbf{r}_j^-) I_{N_j}(T_k^-, \mathbf{r})) \right] \quad (3.33)$$

Mackenzie's basis

$$\mathbf{A}_k(\mathbf{r}) = \frac{\mu}{4\pi l_k} \int_S \frac{\mathbf{g}_k}{|\mathbf{r} - \mathbf{r}'|} ds' \quad (3.34)$$

Splitting over the two neighboring triangles of edge k :

$$\mathbf{A}_k(\mathbf{r}) = \frac{\mu}{4\pi l_k} \left(\hat{\mathbf{d}}_k^+ \int_{S_k^+} \frac{1}{|\mathbf{r} - \mathbf{r}'|} ds' + \hat{\mathbf{d}}_k^- \int_{S_k^-} \frac{1}{|\mathbf{r} - \mathbf{r}'|} ds' \right) \quad (3.35)$$

The integrals appearing in 3.35 have already been analytically expanded in the section to them dedicated, therefore:

$$\mathbf{A}_k(\mathbf{r}) = \frac{\mu}{4\pi l_k} \left[\hat{\mathbf{d}}_k^+ I_1(S_k^+, \mathbf{r}) + \hat{\mathbf{d}}_k^- I_1(S_k^-, \mathbf{r}) \right] \quad (3.36)$$

Figure 3.8 shows the geometry of the case.

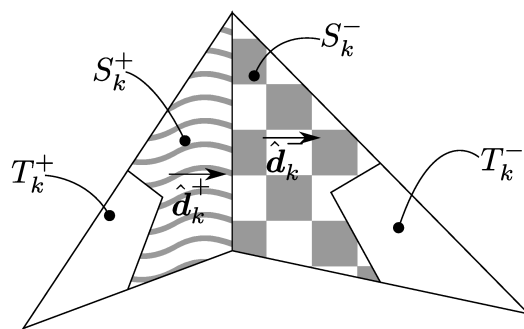


Figure 3.8: Geometry for Mackenzie's magnetic vector potential evaluation.

Chapter 4

Benchmarking

The developed code has been tested against several analytical and numerical results, obtaining good agreement most of the times. In this chapter the validation procedure is detailed following problems of increasing complexity, using the RWG current basis. Key differences with respect to Mackenzie's will be highlighted, with a final section about artifacts that have consistently been found in frequency sweeps.

PEEC is particularly apt at problem complexity reduction. There might be situations where the resistive nature of the problem of interest is negligible, in this cases it is convenient to exclude resistive parameters from the final formulation. A concise notation has been devised to address the many different possible PEEC models. For example, a complete full-wave model is referred to as (Lp, Pp, Rp, τ) PEEC, while, the notation (Pp, Rp) PEEC means that it includes partial coefficients of potential Pp and resistances Rp .

4.1 Resistive code

The first test has been run to confirm the correctness of resistive terms. The theoretical resistance of a conductive slab from Ohm's law (4.1) has been compared to the numerical result obtained through a 772 triangle irregular mesh shown in figure 4.1. The copper slab analysed is 30 cm long, 10 cm wide and 1 μ m thick. The resistance obtained through PEEC has a 2% error from the theoretical 50 m Ω , presumably due to the poor modelling of end connections.

$$R = \rho \frac{l}{wt} \quad (4.1)$$

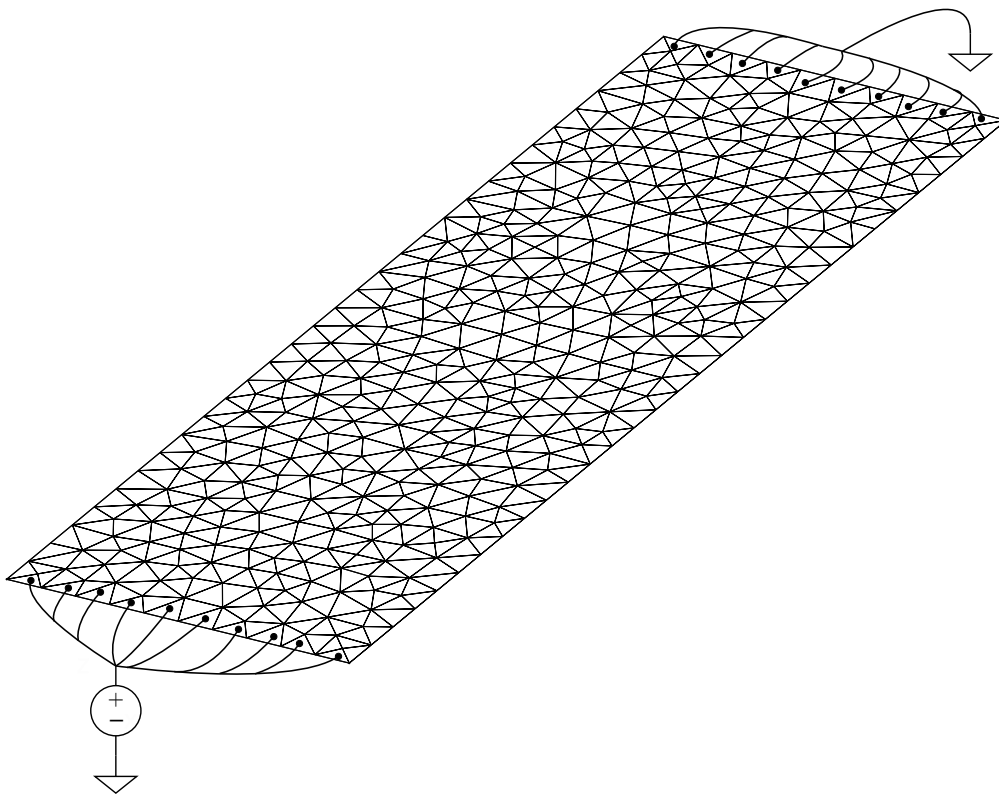


Figure 4.1: Meshed slab's end connections modelling.

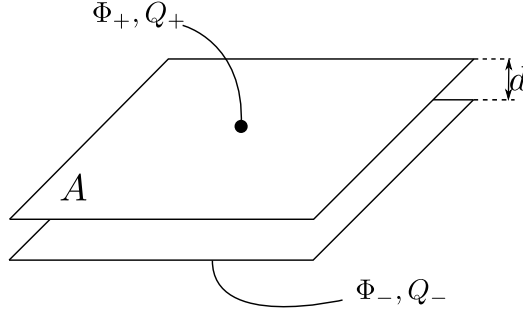


Figure 4.2: Parallel plate capacitor.

4.2 Capacitive code

The partial coefficients of potential have been tested through the study of a parallel square plate capacitor, 10 cm sides and 1 μm air gap. Figure 4.2 depicts the structure (not to scale).

The evaluation of the capacitance has been performed reducing the inverse of the partial coefficient of potential matrix to the short circuit capacitance matrix. The size of this short circuit capacitances matrix is given by the number of physical conductors, quite fewer than the number of partial conductors. The starting point of the computation is the relationship between charges and potentials of the subdivided system given by the partial coefficient of potential matrix.

$$\begin{bmatrix} Pp_{11} & Pp_{12} & \cdots & Pp_{1M} \\ Pp_{21} & Pp_{22} & \cdots & Pp_{2M} \\ \vdots & \vdots & \ddots & \vdots \\ Pp_{M1} & Pp_{M2} & \cdots & Pp_{MM} \end{bmatrix} \begin{bmatrix} Q_1 \\ Q_2 \\ \vdots \\ Q_M \end{bmatrix} = \begin{bmatrix} \Phi_1 \\ \Phi_2 \\ \vdots \\ \Phi_M \end{bmatrix} \implies \mathbf{PpQ} = \Phi \quad (4.2)$$

Inverting 4.2 and denoting with \mathbf{Csp} , the partial short circuit capacitance matrix, the inverse of \mathbf{Pp} , 4.3 can be written.

$$\mathbf{Q} = \mathbf{Pp}^{-1} \Phi \implies \mathbf{Q} = \mathbf{Csp} \Phi \quad (4.3)$$

Next step is to reduce by column 4.3 noticing that the elements of the potential vector can assume only two values for the capacitor of figure 4.2: the potential of the upper plate Φ_+ or the potential of the lower plate Φ_- . Columns can be added together transforming the M by M in an M by 2 matrix.

If only the total charges of the plates are of interest, the system of equations can be further reduced, adding the left-hand side charges together,

which translates in adding together the rows of \mathbf{Csp} . The result is the short circuit capacitance matrix \mathbf{Cs} relating the charges and potentials of physical conductors.

$$\begin{bmatrix} Q_+ \\ Q_- \end{bmatrix} = \begin{bmatrix} C_{s_{++}} & C_{s_{+-}} \\ C_{s_{-+}} & C_{s_{--}} \end{bmatrix} \begin{bmatrix} \Phi_+ \\ \Phi_- \end{bmatrix} \quad (4.4)$$

Solving 4.4 for equal and opposite values of potentials ($\Phi_+ = -\Phi_-$) and using the capacitance definition $C = \frac{Q_+}{\Phi_+}$, the researched value can be easily found.

For the parallel plate capacitor detailed at the beginning of the section a numerical result of 88 nF has been obtained which substantially coincides with the theoretical result computed with the infinite parallel plate approximation (formula 4.5).

$$C = \varepsilon \frac{A}{d} \quad (4.5)$$

4.3 Inductive code

The correctness of partial inductances has been proved simulating the structure of figure 4.3 (not to scale), which is made up of two conductors: a strip 20 cm long and a square loop of 10 mm sides whose center is placed 10 mm away from the axis of the strip. The loop is not completely closed and exhibits a millimeter gap, the voltage across this gap induced by a current flowing in the strip represents the parameter of comparison. On the other side, the benchmark is represented by the voltage computed analytically, approximating the strip as infinitely long and the loop as completely closed. The formula 4.6 returns 14 mV with an excitation of 1 A at a frequency of 1 MHz. PEEC returns the same with no substantial difference.

$$V_{gap} = \omega I \frac{\mu_0 l}{2\pi} \ln \left(\frac{r + \frac{l}{2}}{r - \frac{l}{2}} \right) \quad (4.6)$$

4.4 Quasi-static code

The effectiveness of the quasi-static code, that relays on the parameters tested in the previous sections, has been proved against a consolidated code and approach. The computed input impedance of a transmission line (figure 4.4) has been compared to the result reported in [20]. The finite ground plane is

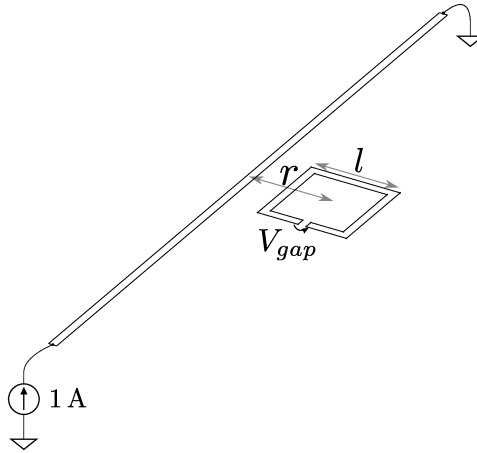


Figure 4.3: Testing structure for partial inductances.

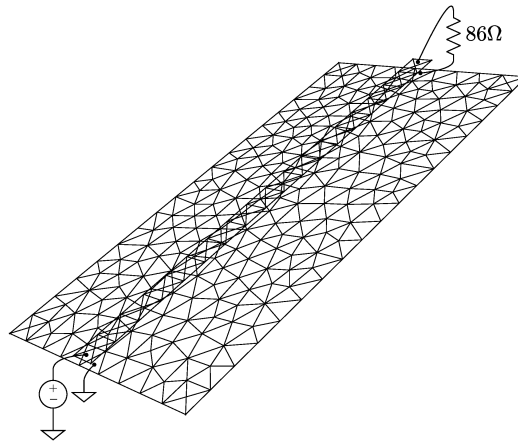


Figure 4.4: Meshed transmission line.

2 cm long by 1 cm wide. The line, placed 0.5 mm above the ground plane, is 2 cm long with a width of 1 mm. It is terminated by an 86Ω resistor.

Frequency sweeps for the input impedance are reported in figure 4.5. The careful eye will spot an artifact around 5 GHz, appearing in otherwise good results. The discussion about these artifacts, as anticipated, will be delayed to a later section.

4.5 Full-wave code

The assessment of correctness of the developed (Lp, Pp, R, τ) PEEC will be presented through the structure of figure 4.6: a conductive strip over a split

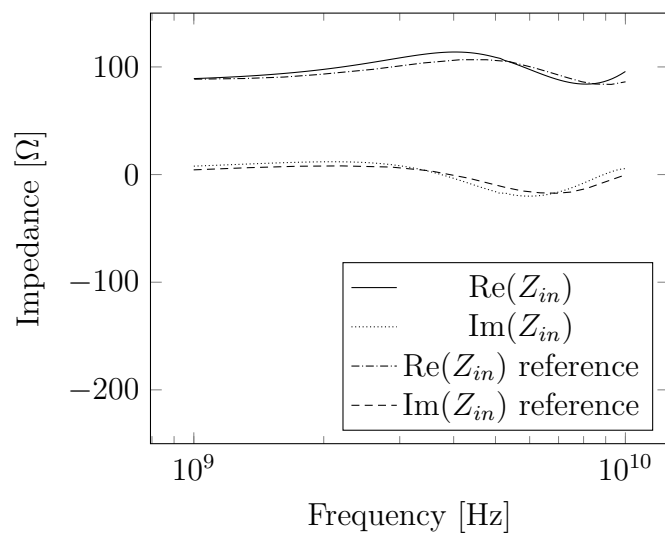


Figure 4.5: Input impedance for the structure of figure 4.4 with RWG.

ground plane.

Results relative to the input impedance in the range 1 – 10 GHz are available in [20], obtained by the standard PEEC method. The dimensions and discretization for this geometry are the same as the quasi-static example, except that the ground plane is now split into two equal halves with 1 mm gap. Figure 4.7 shows the input impedance of the line for this case together with the referenced result.

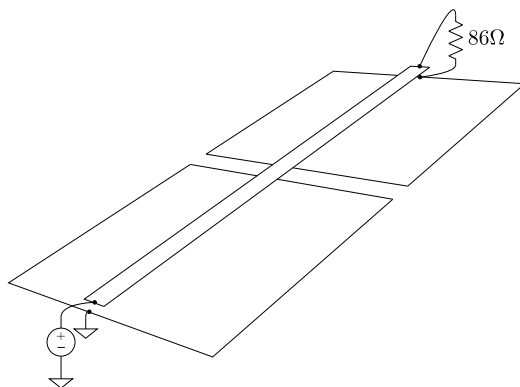


Figure 4.6: Conductive strip above a split ground plane.

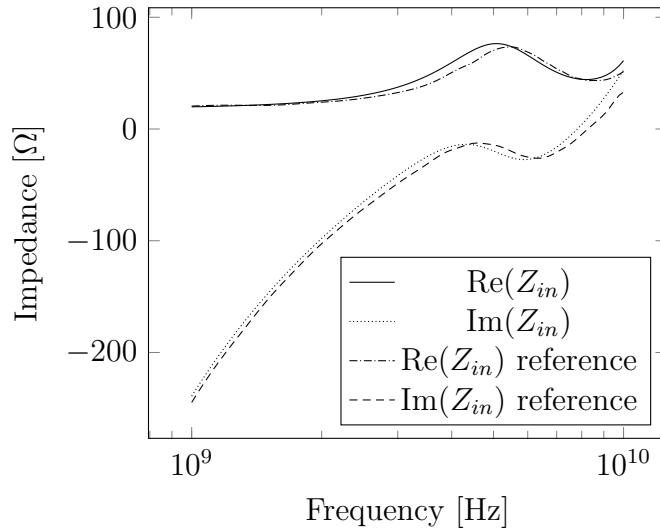


Figure 4.7: Input impedance for the structure of figure 4.6 with RWG.

4.6 Mackenzie's code

The code employing Mackenzie for the current density basis has shown pretty consistent with RWG. It was with great surprise to find out good results for the resistive case, given Mackenzie's highly distorted representation of the current density. The other cases followed along, thing that led to exclude much of this testing from the thesis to avoid dull repetition. The exception has been the inductive one, which will be briefly addressed.

4.6.1 Inductive code

Triangles are not suited to model structures that extend predominantly in one direction, for which rectangles should be preferred whenever possible. The use of Mackenzie's basis for current density emphasizes the problem even more. The consequence is that the testing of the inductive parameters through the structure of figure 4.3 becomes not as straightforward as it was for RWG. Some considerations regarding the distribution of the current along the conducting strip need to be done in order to extract useful information from the PEEC simulation. In this case, the current density is theoretically constant along and across the strip, a distribution that cannot be correctly represented by the use of Mackenzie's basis. These situations are common in EM problems, therefore the possibility of representing a constant field is often one of the proprieties required to a basis (for example: RWG).

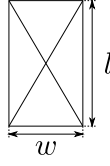


Figure 4.8: Meshed rectangle.

For all these reasons, a parameter c that measures how well the Mackenzie's basis approximates the constant current density distribution is being introduced. c will be employed to correct the mutual inductance computed from the raw output of the simulation, hence it will be referred to as the correction factor in the following discussion.

$$c = \frac{|\int_X \mathbf{J} ds|}{|A_X \mathbf{J}_{th}|} \quad (4.7)$$

where X is any triangle or compound thereof over which there should be a theoretically constant current density \mathbf{J}_{th} , while A_X is its area. It can be noted that 4.7 gives an error in terms of module, however there could generally even be an error of direction, possibly described defining another parameter.

The conducting strip of figure 4.3 is regularly meshed stacking up rectangles which are split in triangles as in figure 4.8. In this case, c is computed over the rectangle considering that the segments connecting the centroid to the edge midpoints divide a triangle in three equal area quadrangles and that the current density flowing past the oblique interior edges is $\frac{w}{\sqrt{w^2+l^2}}$ the one passing the interior edges cutting the strip perpendicularly. The correction factor evaluates as follows.

$$c = \frac{1}{3} + \frac{4}{3} \frac{w^2}{w^2 + l^2} \quad (4.8)$$

From the formula 4.8, global correspondence between theoretical and discretized distributions can only be evinced when $w = l$, with a unitary value for c .

The mutual inductance for the structure 4.3 is extracted from the numerical results of the PEEC simulation dividing the induced voltage in the loop by the current in the conducting strip and the angular frequency at which the simulation is performed. The numerical results are plotted in figure 4.9 against the theoretical value, varying the number of meshing rectangles.

It has been verified that the nature of the loop mesh doesn't substantially alter the simulation output. For this reason, it has been chosen once and kept

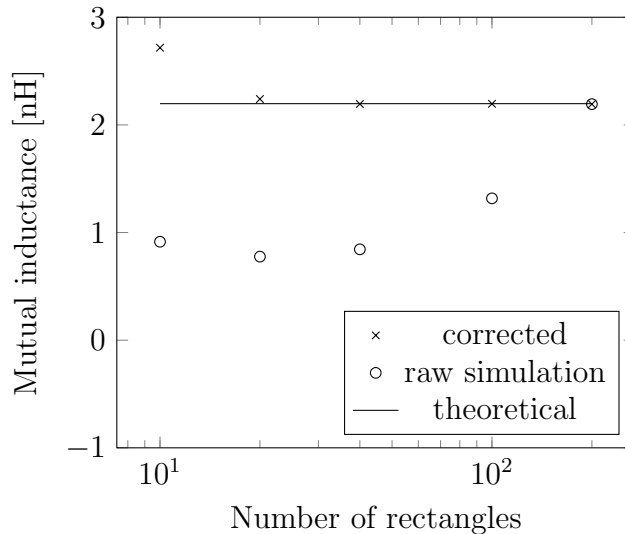


Figure 4.9: Mutual inductance of structure 4.3.

constant while varying the mesh of the conducting strip.

From figure 4.9, it emerges that the simulation results are not directly comparable to the theoretical results, except from the last one. The reason is to be researched in the misrepresentation of the current density, which determines the magnetic vector potential hence the voltage induced in the loop. The factor c , which can be loosely interpreted as the ratio between the numerical and theoretical current densities, can be directly employed to correct the mutual inductance. Dividing the “raw simulation” data by the correction factor, a new series is obtained appearing immediately more coherent to the theory.

4.7 Frequency sweep artifacts

During testing odd artifacts in frequency sweeps have been verified to appear for both current density bases. Some attempts to find their cause ended with no luck. The time at disposal and the available knowledge hasn’t been enough to find a satisfactory explanation, which would require a more thorough investigation. Other works on standard PEEC have reported similar anomalies, for instance [21].

To get a better grasp of their nature, consider Pinello’s transmission line already described in the RWG quasi-static code section. Figure 4.10 shows an analogous benchmarking but using Mackenzie’s basis, which has been obtained sampling the waveforms with irregularly spaced points. In particular,

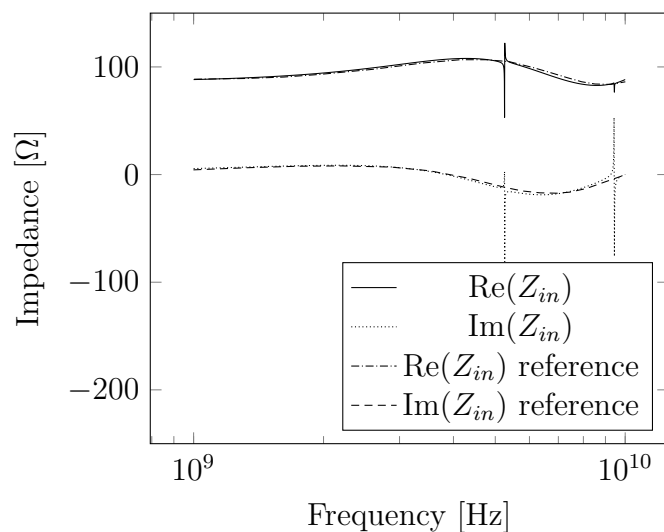


Figure 4.10: Input impedance for Pinello's transmission line with Mackenzie's basis.

around the spotted singularities, a finer frequency step has been employed in order to catch the sharp variations. Smaller singularities could hide in correspondence of the apparently smoother sections where a coarser sampling has been adopted. These artifacts alter the waveform only locally which makes their detection harder, as is the case for figure 4.5. Another feature is that they seem more pronounced when propagation delays are not included, see figure 4.11 where the introduction of delays clears the problem.

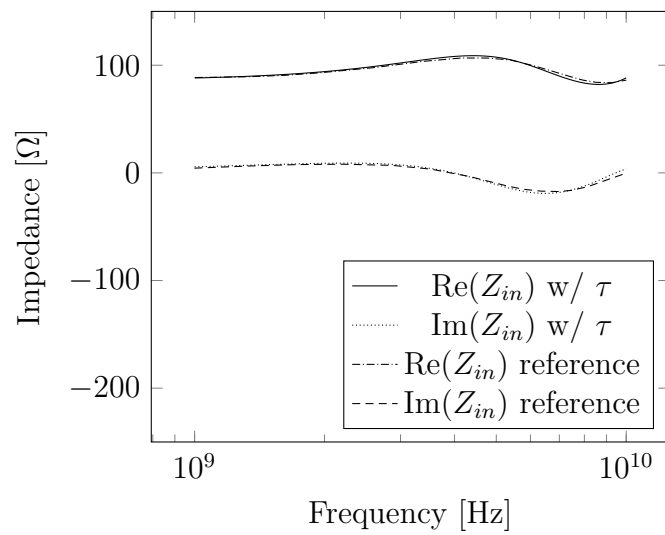


Figure 4.11: Input impedance for Pinello's transmission line with Mackenzie's basis and delays.

Chapter 5

Implementation and Performance analysis

For this thesis, roughly 4000 lines of code were written, of which 1500 make up the computational kernel available on GitHub, [22], in the form of C library.

The PEEC solver has been structured covering the back-end section of the flow chart in figure 5.1.

The front-end has been left to third-party software. All the examples in the benchmarking chapter and the still-to-come RF coil study have been performed using GMSH, [23], for geometry description and meshing, and Paraview, [24], for output visualization. Different choices are possible provided that data is passed to the back-end in the legacy ASCII VTK file format, which has been chosen for ease of programming.

As now, setting up an EM problem is quite cumbersome, user interface would greatly benefit from a review.

Now the two more computationally expensive stages in the code will be discussed.

5.1 Partial element computation

The evaluation of partial elements has noticeable effects on computational time only at low number of faces. In fact, its algorithm is $O(n^2)$, quickly overshadowed by the solution stage ($O(n^3)$). n could be taken to be the number of triangular faces or interior edges considering that in well-behaved structures a ratio of $\frac{3}{2}$ exists between them.

As already detailed, two different current density bases have been considered: RWG and Mackenzie. Before the beginning of the thesis, it was

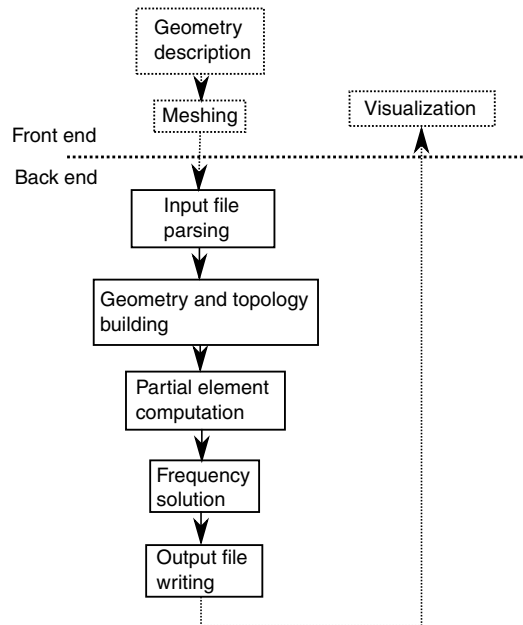


Figure 5.1: Flow chart of the developed PEEC code.

thought that a conceptually simpler basis as Mackenzie would have led to a speed up. As figure 5.2 demonstrates, the assumption has been proven wrong.

A fair amount of work needs to be done every time the integration domain is being switched. In the case of RWG, this amount of work is performed once for each triangular face, while in the case of Mackenzie it has to be timed by four, with an inevitable increase in number of operations.

In conclusion, unless a completely different approach is devised, the use of Mackenzie's basis can be considered no more than an academic exercise. Practical applications should prefer RWG basis which is faster and better approximates current density, \mathbf{J} .

The core library has been multi-threaded making use of OpenMP, [25], which has been chosen for its portability and simplicity.

One typically has to call platform-specific routines in order to get multi-threading. In a POSIX environment, where this PEEC code has been tested, the alternative would have been pthreads, for example not portable on Windows.

The use of OpenMP is almost as simple as putting

```
#pragma omp parallel for
```

in front of the for loops that are intended to work in parallel.

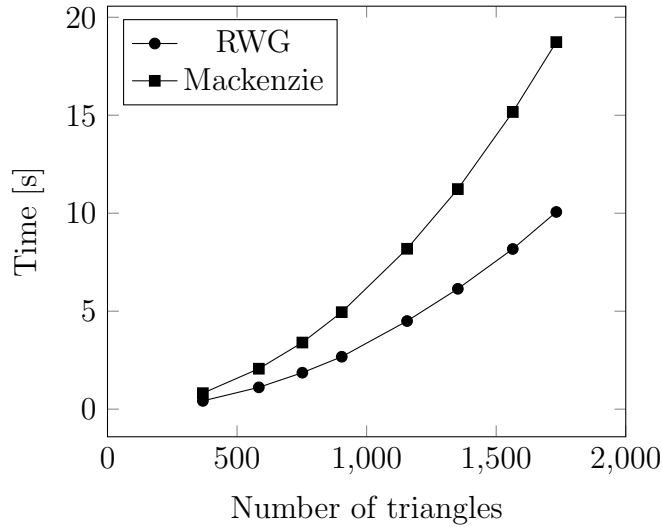


Figure 5.2: Times for single-thread computation of partial elements.

The only downside to the use of OpenMP is that the compiler has to support it.

Figure 5.3 highlights the improvement brought by multi-threading, comparing times for the evaluation of partial elements against the library compiled as a single-thread. The test was run on a dual core CPU.

5.2 Frequency solution

The frequency solution stage dominates the overall computational time and is comprised of a for loop over the frequency samples. For each sample the final linear system is assembled and then solved. The direct method solution with a time complexity of $O(n^3)$ represents the limitation to the PEEC code, which can be partially soothed exploiting problem symmetries.

The possibility to include rectangular symmetries in the form of a command line option has been added to the developed code. The following is an example invocation in which the maximum number of symmetries is specified: three, one for each plane of the orthogonal 3D space, together with proper sign (positive or negative).

```
peec -sx+y+z- infile.vtk outfile.vtk
```

Each symmetry halves the number of unknowns, which means that the solution time can be reduced by a total top factor of 512, figure 5.4 is proof. The linear system solution times for a parallel plate capacitor with and with-

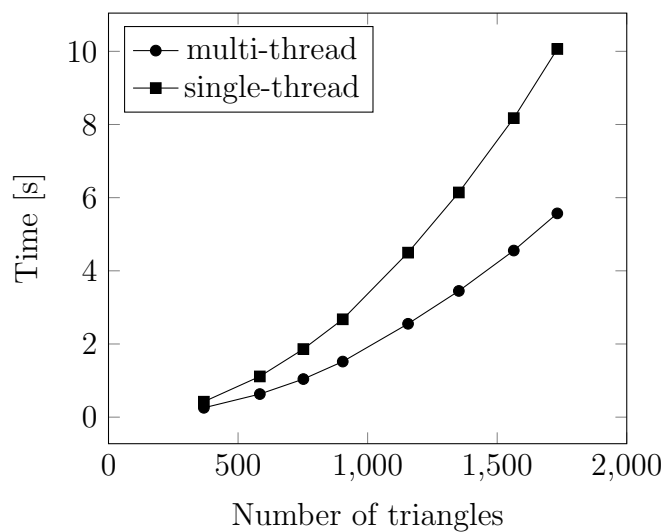


Figure 5.3: Times for single and multi-thread computation of partial elements.

out symmetries are compared. Despite these promising results, it's hard to find problems with more than a symmetry; the parallel plate capacitor should be regarded as a fortunate case.

Symmetries have effects on memory allocation (64 top reduction factor) and on partial elements evaluation time (8 top reduction factor) as well.

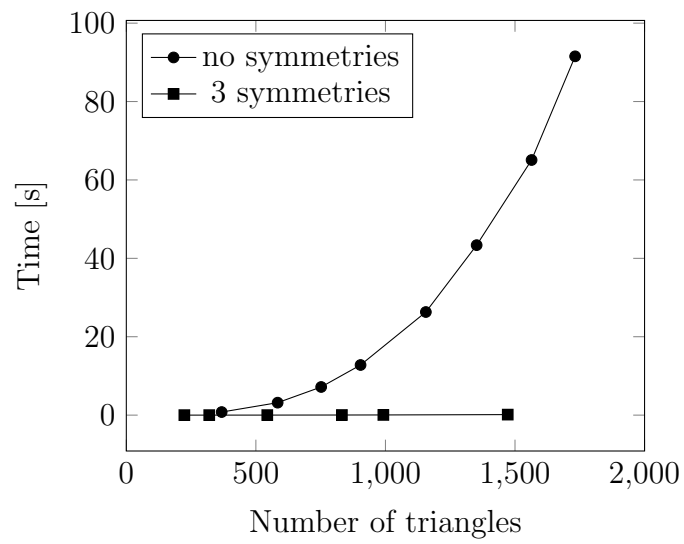


Figure 5.4: Linear system solution times for a frequency sample.

Chapter 6

RF coils

In MRI (Magnetic Resonance Imaging), RF coils are any of the radiating structures for both transmission and reception operating in the radio frequency slice of the spectrum. The explanation of the role they play in the imaging process will not be detailed, in part, because it would take some chapters only by itself, but mostly because several good resources already exist, for example [26], along with a valuable series of Youtube video-lectures.

Said that, a bit of an introduction is still required. The term coil which will be used throughout the chapter can lead to erroneous interpretations, in fact, in the field it's not unusual to see it applied to structures that nothing have to do with the coils that an electrical engineer is used to. In the early days of MRI, coils were the only mean to convey RF radiations on a sample under study, even today they are widely in use, as a consequence the term has become a synecdoche for any RF structure.

The object of this study is a 12-element microstrip array employed as RF radiating apparatus in MR head imaging at 7 T, corresponding to 300 MHz in precessional frequency of protons. The microstrips making up the array are ideally laid along and on the exterior of a 300 mm diameter cylinder, projecting the majority of their magnetic field inside. Each element is 200 mm long and the conducting strip contacting the cylinder is 20 mm wide, supported on a 10 mm dielectric substrate of Teflon, with a dielectric constant of 2.1. This substrate extends 60 mm in width and is being backed up on its entire external surface by a thin layer of copper, working as ground plane. Beside the essential structure just described, an additional cylindrical conductive shield 380 mm in diameter is employed such that it encloses the RF coils and separates them from the gradient coils. The complete structure is pictured in figure 6.1.

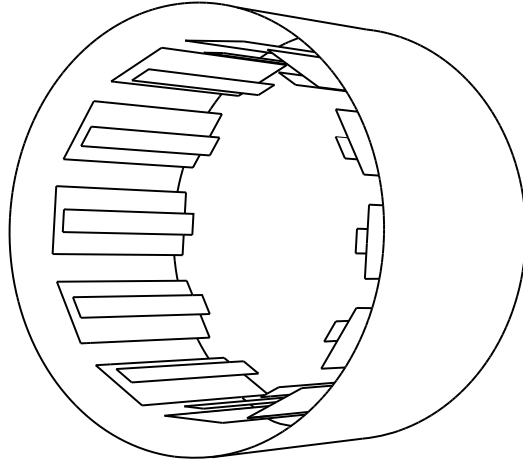


Figure 6.1: 12-channel microstrip RF coil array.

6.1 Microstrip parameters

In the pre-computer era a number of analytical formulae for the analysis and synthesis of microstrip lines have been proposed. This section focuses on the characteristic impedance, Z_0 , and the effective relative permittivity, ε_e , which are also the electrical parameters that received the most attention in scientific literature. ε_e arises from the modelling of the microstrip as it was surrounded by an homogeneous dielectric medium.

The arguably most cited set of equations are those reported by Erik O. Hammerstad in [27], where he revises on the work of H. A. Wheeler, [28], and M. V. Schneider, [29]. The success of this formulation is probably due to the conciseness of the expressions reported in 6.1 and 6.2, and the full adherence to the modelling abstraction of the equivalent homogeneous dielectric medium.

$$Z_0 = \begin{cases} \frac{60}{\sqrt{\varepsilon_e}} \ln \left(8 \frac{h}{w} + \frac{w}{4h} \right), & \text{when } \frac{w}{h} \leq 1 \\ \frac{120\pi}{\sqrt{\varepsilon_e} \left[\frac{w}{h} + 1.393 + 0.667 \ln \left(\frac{w}{h} + 1.444 \right) \right]}, & \text{when } \frac{w}{h} \geq 1 \end{cases} \quad (6.1)$$

where

$$\varepsilon_e = \frac{\varepsilon_r + 1}{2} + \frac{\varepsilon_r - 1}{2} \left(\frac{1}{\sqrt{1 + 12 \left(\frac{h}{w} \right)}} \right). \quad (6.2)$$

These equations are the product of several approximations performed by different authors and a mixture of analytical and numerical elaborations, whose detailed explanation is beyond the scope of this thesis. The interested reader can start by referring to the cited articles.

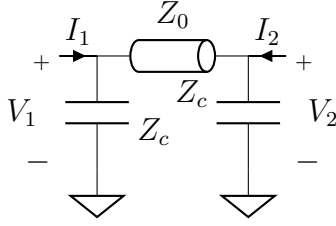


Figure 6.2: Spice model of the microstrip RF coil.

6.2 Microstrip coil design

Microstrip coils are designed to be operated at resonant frequencies, which translates as a constraint on their length. However, this condition can be easily relaxed through the use of capacitors or inductors at both ends of the line. Inductors which, indeed, represent a theoretical possibility are not used in practice. Equal values of capacitance are usually employed as to keep the magnetic field symmetric and the region of higher intensity in the center of the line.

With some transmission line theory it is possible to derive equation 6.3 for the input impedance of a capacitively shunted microstrip, whose equivalent circuit is shown in figure 6.2.

$$Z_{\text{in}} = \frac{Z_C Z_0 (Z_C + j Z_0 \tan(\beta l))}{2 Z_0 Z_C + j (Z_C^2 + Z_0^2) \tan(\beta l)} \quad (6.3)$$

where β is the phase constant:

$$\beta = \frac{\omega_0 \sqrt{\epsilon_e}}{c} \quad (6.4)$$

c is the speed of light in vacuum or air and $\omega_0 = 2\pi f$ is the angular Larmor frequency of protons.

Two types of resonance are possible, one is the series resonance condition typical of dipole antennae, reached when the reactance component of the input impedance equals zero. The other, parallel resonance, is practical in RF coils, where the susceptance part of the input admittance is required to be zero, [30]. For the case under study, this latter condition is reached, with reference to equation 6.3, at a particular value of capacitance.

$$C = \frac{\sin(\beta l)}{\omega_0 Z_0 (1 - \cos(\beta l))} \quad (6.5)$$

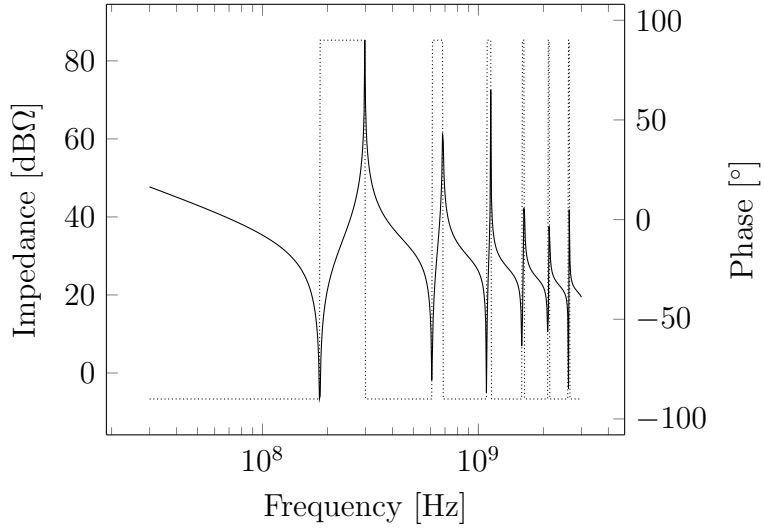


Figure 6.3: Spice-simulated RF coil $Z_{11}(Z_{22})$: magnitude and phase.

6.3 Coil characterization

The coil, described in the introductory part of the chapter, shunted with capacitances, as computed from the formulae of the previous section, has been simulated through the developed PEEC code.

Before that, a Spice simulation has been run to get a fast approximation. The results, in the form of impedance matrix, can be found plotted in figure 6.3 and 6.4, together with the used netlist in appendix B.

$$\begin{bmatrix} V_1 \\ V_2 \end{bmatrix} = \begin{bmatrix} Z_{11} & Z_{12} \\ Z_{21} & Z_{22} \end{bmatrix} \begin{bmatrix} I_1 \\ I_2 \end{bmatrix}, \quad Z_{11} = Z_{22}, \quad Z_{21} = Z_{12} \quad (6.6)$$

The resistivity of conductors has not been taken into account in Spice as well as in PEEC, in fact, data regarding the thickness of conductors was missing. The effect of resistive parameters could be negligible, hence their omission justified, but it should be verified for sure.

6.3.1 PEEC results

PEEC results have been obtained on four different configurations of RF coil. Longitudinal cuts have been introduced on the ground plane and on the shield in an attempt to reduce undesired eddy currents generated by gradient coils (figure 6.5). Two additional configurations with cuts selectively on the ground or on the shield are also taken into consideration.

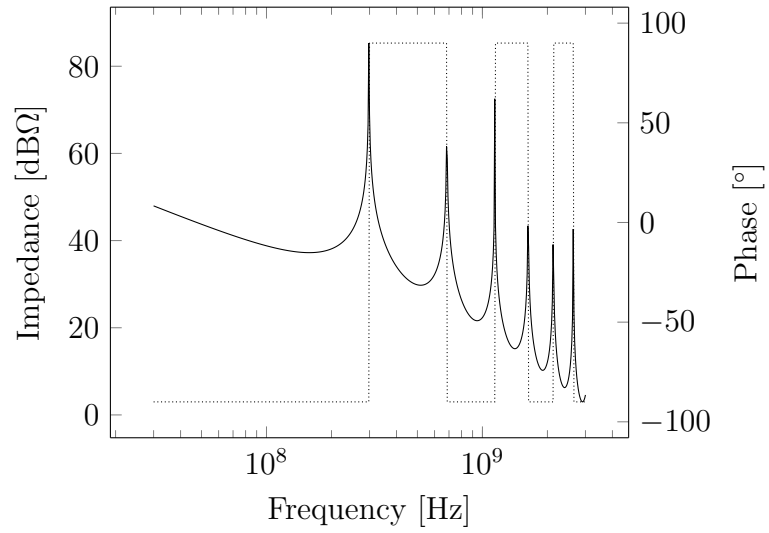


Figure 6.4: Spice-simulated RF coil $Z_{21}(Z_{12})$: magnitude and phase.

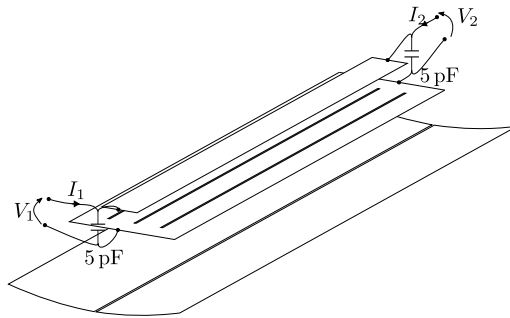


Figure 6.5: RF coil with cuts, external capacitors and ports identified.

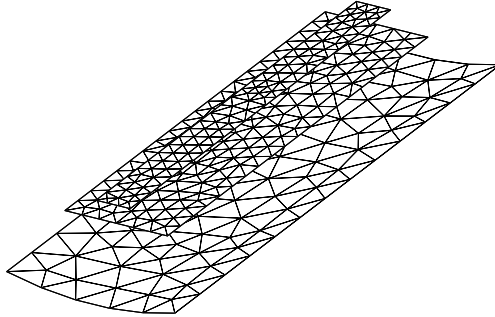


Figure 6.6: Meshed microstrip RF coil without cuts.

Simulating only one twelfth of the complete array has granted the possibility to employ a sufficiently fine mesh (figure 6.6). This is of course an approximation but still necessary with the computational resources at disposal. Also, the use of symmetries wouldn't have helped much, considering the fact there is only one.

Like Spice, PEEC results are reported in figure 6.7 and 6.8 in a similar fashion, however, in this case the waveforms are heavily masked by the artifacts already considered in the benchmarking chapter. Luckily, the lower part of the spectrum up to around 500 MHz, containing the range of frequencies in which the application operates, is free from this problem. A blown-up of Z_{11} is provided in figure 6.9, where the resonance shifting effect exerted by different cuts can be appreciated.

As a final note, it's interesting to highlight how the capacitances which have been tuned on the basis of the equations of the previous section bring the resonance frequency at about 324.9 MHz, instead of the desired 298 MHz. This substantial discrepancy is partly due to the analytical approach, which is based off the two-dimensional approximation of a transmission line, completely neglecting end effects, and partly due to the difficulties of modelling end connections inherent to the PEEC method.

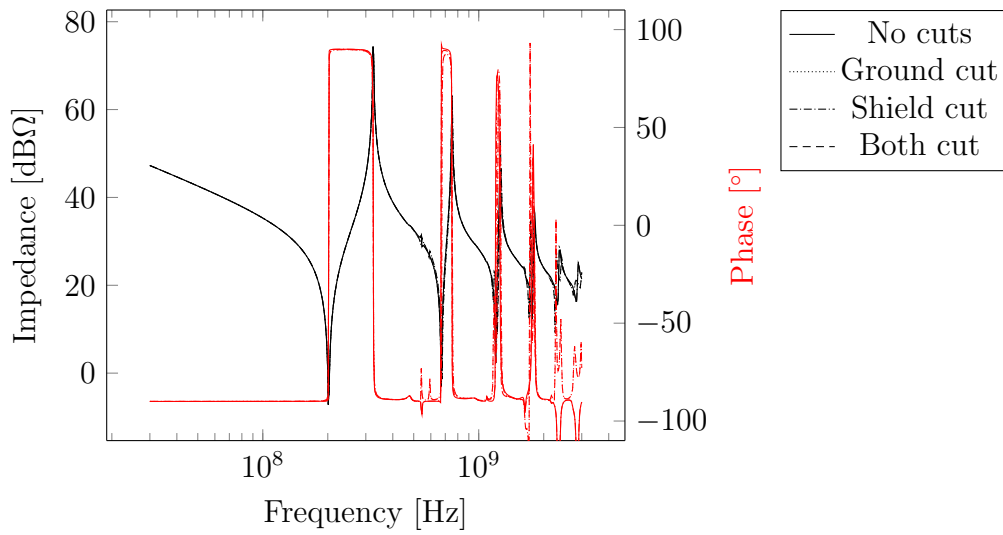


Figure 6.7: PEEC-simulated RF coil $Z_{11}(Z_{22})$: magnitude and phase.

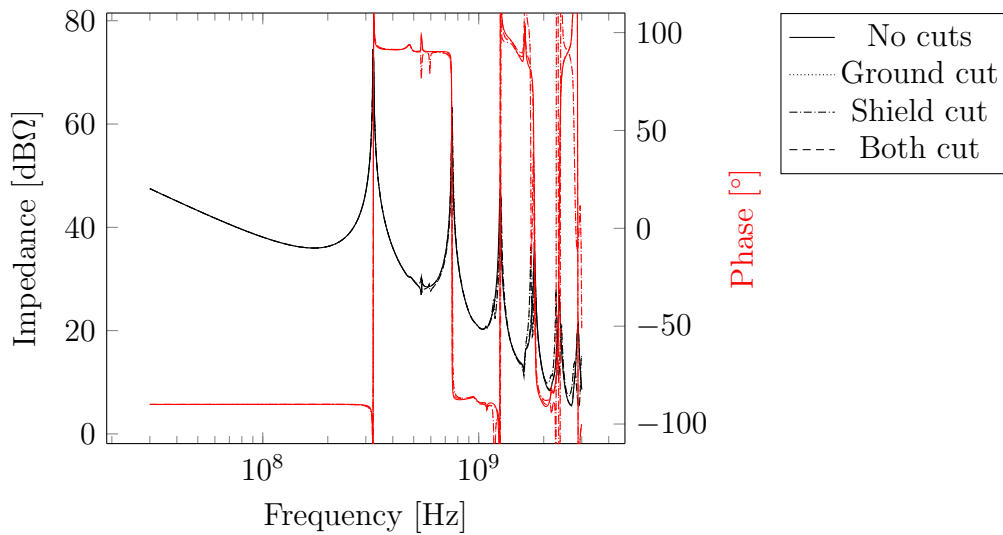


Figure 6.8: PEEC-simulated RF coil $Z_{21}(Z_{12})$: magnitude and phase.

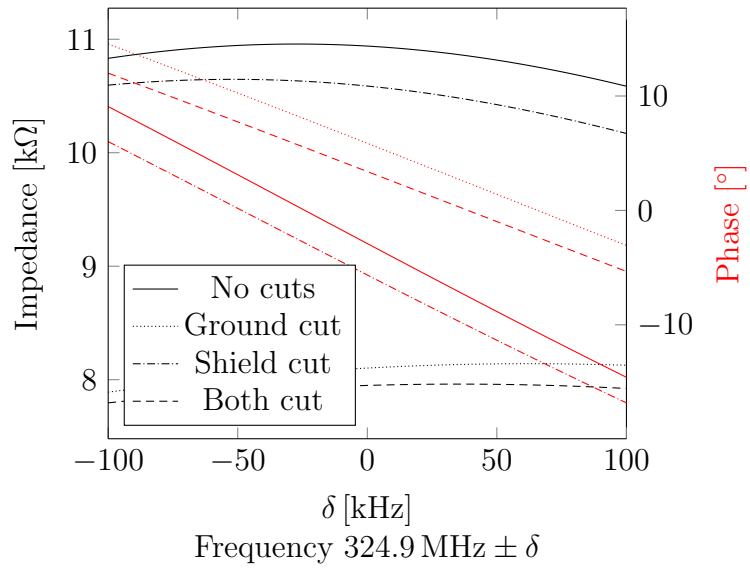


Figure 6.9: Blown-up of $Z_{11}(Z_{22})$ at the resonance frequency for comparison of the RF coils.

Chapter 7

Conclusion

A full-fledged PEEC code has been written and applied to the study of a 12-channel RF coil array of a MRI scanner. The computational kernel, in the form of a C library, has been shared on GitHub, [22], and the related documentation made available through Doxygen, [31].

7.1 Further development

The developed code is surface-based, which has been good enough for the study of the application at hand. It would be interesting to see how the PEEC method behaves with solid structures, in fact, in its simpler form there is the subtle assumption of a dielectric constant homogeneous throughout the space, that is even conductors. This is not a problem with triangles since they do not have a physical volume but could become one with tetrahedra, for example.

For Mackenzie's basis, a new approach for calculating resistive coefficients has been benchmarked with success on different problems, however it lacks some theoretical background, which should be (have been) provided.

Finally, an investigation of the causes leading to the frequency sweep artifacts found in PEEC, could reveal extremely interesting.

Appendix A

Divergence of RWG basis functions

In this appendix will be proved the divergence of the RWG basis function \mathbf{f}_n . Let's begin by writing the divergence in terms of rectangular coordinates.

$$\operatorname{div} \mathbf{f}_n = \frac{\partial \mathbf{f}_n}{\partial x} \cdot \hat{\mathbf{i}} + \frac{\partial \mathbf{f}_n}{\partial y} \cdot \hat{\mathbf{j}} + \frac{\partial \mathbf{f}_n}{\partial z} \cdot \hat{\mathbf{k}} \quad (\text{A.1})$$

Note that \mathbf{f}_n is a piecewise linear function, which means the derivatives with respect to any of its independent variables (x, y, z) as well as $\operatorname{div} \mathbf{f}_n$ will be piecewise constant. The value of $\operatorname{div} \mathbf{f}_n$ on the triangle T_n^+ can be found exploiting Green's theorem.

$$\int_{T_n^+} \operatorname{div} \mathbf{f}_n dv = \int_{\partial T_n^+} \mathbf{f}_n \cdot \hat{\mathbf{n}} ds \quad (\text{A.2})$$

$$\operatorname{div} \mathbf{f}_n A_n^+ dt = l_n dt \quad (\text{A.3})$$

where dt denotes the infinitesimal thickness of the triangle T_n^+ . In the last member the fact that $\mathbf{f}_n \cdot \hat{\mathbf{n}}$ is non null only on the common edge and there assumes unitary value has been leveraged, reducing the integral to the computation of an area, although infinitesimal. The expression for $\operatorname{div} \mathbf{f}_n$ can be finally written.

$$\operatorname{div} \mathbf{f}_n = \frac{l_n}{A_n^+} \quad \text{on } T_n^+ \quad (\text{A.4})$$

Analogously for T_n^- :

$$\operatorname{div} \mathbf{f}_n = -\frac{l_n}{A_n^-} \quad \text{on } T_n^- \quad (\text{A.5})$$

Appendix B

Spice netlist for RF coil simulation

```
1 Microstrip RF coil
2 Tmicro 1 0 2 0 Td=966p Z0=84
3 C1 1 0 5p
4 C2 2 0 5p
5 Vin 1 0 ac 1 0
6 .ac dec 300 30meg 3g
7 * print variables for post-processing Z_11(Z_22) and Z_21(Z_12)
8 .print ac i(Vin) v(2)
9 .end
```

Bibliography

- [1] Dale R. Corson Paul Lorrain. *Electromagnetic fields and waves, including circuits*. Physics Series. W.H. Freeman and Company, 3 sub edition, 1988.
- [2] Menno E. Verbeek. Partial element equivalent circuit (peec) models for on-chip passives and interconnects. *International Journal of Numerical Modelling: Electronic Networks, Devices and Fields*, 17(1):61–84, 2004.
- [3] A. E. Ruehli. Equivalent circuit models for three-dimensional multiconductor systems. *IEEE Transactions on Microwave Theory and Techniques*, 22(3):216–221, Mar 1974.
- [4] University of Berkeley California. Spice download page. <https://embedded.eecs.berkeley.edu/pubs/downloads/spice/>. Accessed: 2017-07-28.
- [5] Ngspice website homepage. <http://ngspice.sourceforge.net/>. Accessed: 2017-07-28.
- [6] Lijun Jiang Albert E. Ruehli, Giulio Antonini. *Circuit Oriented Electromagnetic Modeling using the PEEC Techniques*. IEEE Press / Wiley, 2017.
- [7] Prof. Dr. Gunter Wollenberg Prof. Dr. Juergen Nitsch, Dr. Frank Gronwald. *Radiating Nonuniform Transmission-Line Systems and the Partial Element Equivalent Circuit Method*. 1 edition, 2009.
- [8] G. Antonini, A. E. Ruehli, and J. Esch. Nonorthogonal peec formulation for time and frequency domain modeling. In *2002 IEEE International Symposium on Electromagnetic Compatibility*, volume 1, pages 452–456 vol.1, Aug 2002.
- [9] Aosheng Rong and A. C. Cangellaris. Generalized peec models for three-dimensional interconnect structures and integrated passives of arbitrary

- shapes. In *IEEE 10th Topical Meeting on Electrical Performance of Electronic Packaging (Cat. No. 01TH8565)*, pages 225–228, 2001.
- [10] V. Jandhyala, Yong Wang, D. Gope, and R. Shi. Coupled electromagnetic-circuit simulation of arbitrarily-shaped conducting structures using triangular meshes. In *Proceedings International Symposium on Quality Electronic Design*, pages 38–42, 2002.
- [11] S. Rao, D. Wilton, and A. Glisson. Electromagnetic scattering by surfaces of arbitrary shape. *IEEE Transactions on Antennas and Propagation*, 30(3):409–418, May 1982.
- [12] F. Freschi and Maurizio Repetto. A general framework for mixed structured/unstructured peec modelling. 23:200–206, 09 2008.
- [13] Anne I. Mackenzie and Michael E. Baginski. New basis functions for the electromagnetic solution of arbitrarily-shaped, three dimensional conducting bodies using method of moments. 2005.
- [14] A. Glisson and D. Wilton. Simple and efficient numerical methods for problems of electromagnetic radiation and scattering from surfaces. *IEEE Transactions on Antennas and Propagation*, 28(5):593–603, Sep 1980.
- [15] H. Heeb and A. E. Ruehli. Three-dimensional interconnect analysis using partial element equivalent circuits. *IEEE Transactions on Circuits and Systems I: Fundamental Theory and Applications*, 39(11):974–982, Nov 1992.
- [16] Roger F. Harrington. *Field Computation by Moment Methods (IEEE Press Series on Electromagnetic Wave Theory)*. The IEEE PRESS Series in Electromagnetic Waves (Donald G. Dudley, Editor). Wiley-IEEE Press, 1993.
- [17] F. Freschi, G. Gruosso, and M. Repetto. Unstructured peec formulation by dual discretization. *IEEE Microwave and Wireless Components Letters*, 16(10):531–533, Oct 2006.
- [18] D. Wilton, S. Rao, A. Glisson, D. Schaubert, O. Al-Bundak, and C. Butler. Potential integrals for uniform and linear source distributions on polygonal and polyhedral domains. *IEEE Transactions on Antennas and Propagation*, 32(3):276–281, Mar 1984.

- [19] Roberto D. Graglia. On the numerical integration of the linear shape functions times the 3-d green's function or its gradient on a plane triangle. 41:1448 – 1455, 11 1993.
- [20] W. Pinello, A. C. Cangellaris, and A. Ruehli. Hybrid electromagnetic modeling of noise interactions in packaged electronics based on the partial-element equivalent-circuit formulation. *IEEE Transactions on Microwave Theory and Techniques*, 45(10):1889–1896, Oct 1997.
- [21] J. Ekman and G. Antonini. On characterizing artifacts observed in peec based modeling. In *2004 International Symposium on Electromagnetic Compatibility (IEEE Cat. No.04CH37559)*, volume 1, pages 251–255 vol.1, Aug 2004.
- [22] Libpeec code repository. <https://github.com/albertoscotta/libpeec>. Accessed: 2018-02-03.
- [23] Christophe Geuzaine and Jean-François Remacle. Gmsh: A 3-D finite element mesh generator with built-in pre- and post-processing facilities. *International Journal for Numerical Methods in Engineering*, 79:1309 – 1331, 2009.
- [24] Utkarsh Ayachit. *The ParaView Guide: A Parallel Visualization Application*. Kitware, Inc., USA, 2015.
- [25] OpenMP website homepage. <http://www.openmp.org/>. Accessed: 2018-02-10.
- [26] Micheal L. Lipton. *Totally Accessible MRI A User's Guide to Principles, Technology, and Applications*. Springer-Verlag New York, 1 edition, 2008.
- [27] E. O. Hammerstad. Equations for microstrip circuit design. In *1975 5th European Microwave Conference*, pages 268–272, Sept 1975.
- [28] H. A. Wheeler. Transmission-line properties of parallel strips separated by a dielectric sheet. *IEEE Transactions on Microwave Theory and Techniques*, 13(2):172–185, Mar 1965.
- [29] M. V. Schneider. Microstrip lines for microwave integrated circuits. *The Bell System Technical Journal*, 48(5):1421–1444, May 1969.
- [30] Carl Snyder. *TEM Arrays, Design and Implementation*. John Wiley & Sons, Ltd, 2007.

[31] Doxygen website homepage. <http://www.doxygen.org>. Accessed: 2018-02-03.